R *INRIA*

INSTITUT NATIONAL DE RECHERCHE EN INFORMATIQUE ET EN AUTOMATIQUE

Time-consistent estimators of 2D/3D motion of atmospheric layers from pressure images

Patrick Héas — Nicolas Papdakis — Etienne Mémin

N° 6292

Juin 2007

R *apport*
de recherche

Time-consistent estimators of 2D/3D motion of atmospheric layers from pressure images

Patrick Héas , Nicolas Papdakis , Etienne Mémin

Abstract: In this paper, we face the challenging problem of estimation of time-consistent layer motion fields at various atmospheric depths. Based on a vertical decomposition of the atmosphere, we propose three different dense motion estimator relying on multi-layer dynamical models. In the first method, we propose a mass conservation model which constitutes the physical background of a multi-layer dense estimator. In the perspective of adapting motion analysis to atmospheric motion, we propose in this method a two-stage decomposition estimation scheme. The second method proposed in this paper relying on a 3D physical model for a stack of interacting layers allows us to recover a vertical motion information. In the last method, we use the exact shallow-water formulation of the Navier-Stokes equations to control the motion evolution across the sequence. This is done through a variational approach derived from data assimilation principle which combines the dynamical model and the pressure difference observations obtained from satellite images. The three methods use sparse pressure difference image observations derived from top of cloud images and classification maps. The proposed approaches are validated on synthetic example and applied to real world meteorological satellite image sequences.

Key-words: Motion estimation; variational methods; optimal control; optical-flow; 3D atmospheric dynamics; physical-based methods

Estimateurs temporellement cohérents de mouvements 2D/3D de couches atmospheriques partir d'images de pression

Résumé :   Ce papier aborde le problème ambitieux de l'estimation de champs de mouvements temporellement cohérents de couches atmosphériques à différentes altitudes. Basé sur la décomposition verticale de l'atmosphère, nous proposons trois différents estimateurs denses de mouvement en s'appuyant sur un modèle dynamique stratifié. Pour la première méthode, nous proposons un modèle de conservation de la masse qui constitue la base physique d'un estimateur dense stratifié. Dans l'optique d'adapter l'analyse du mouvement au flot atmosphérique, nous proposons une décomposition en deux étapes de l'estimation de mouvement. La deuxième méthode proposée dans ce papier permet de recouvrer la composante verticale du mouvement en s'appuyant sur la physique tri-dimensionnelle d'un empilement de couches interconnectées. Dans la dernière méthode, on utilise la formulation exact du modèle des eaux peu profondes de Saint Venant pour controler l'évolution des mouvements atmosphériques au cours de la séquence. Ce contrôle est effectué par une approche variationnelle dérivée du principe de l'assimilation de données. Celui-ci permet de combiner la dynamique d'un modèle avec des observations issues de l'imagery satellitaire. Les trois méthodes utilisent des observations éparses de différence de pression qui sont dérivées des images satellitaires de pression au sommet des nuages et des cartes de classifications associées. Les approches sont validées sur des exemples synthétiques et appliquées sur des séquences réelles d'images de satellites météorologiques.

Mots-clés :   Estimation de mouvements; méthodes variationelles; contrôle optimal; flot-optique; dynamique atmospherique 3D; méthodes basées sur la physique

1 Introduction

Geophysical motion characterization and image sequence analysis are crucial issues for numerous scientific domains involved in the study of climate change, weather forecasting, climate prediction or biosphere analysis. The use of surface station, balloon, and more recently in-flight aircraft measurements and low resolution satellite images has improved the estimation of wind fields and has been a subsequent step for a better understanding of meteorological phenomena. However, the network's temporal and spatial resolutions may be insufficient for the analysis of mesoscale dynamics. Recently, in an effort to avoid these limitations, another generation of satellites sensors has been designed, providing image sequences characterized by finer spatial and temporal resolutions. Nevertheless, the analysis of motion remains particularly challenging due to the complexity of atmospheric dynamics at such scales.

Tools are needed to exploit this new generation of satellite images. Nevertheless, in the context of geophysical motion analysis, standard techniques from computer vision, originally designed for bi-dimensional quasi-rigid motions with stable salient features, appear to be not well adapted [14, 16]. The design of techniques dedicated to fluid flow has been a step forward, towards the constitution of reliable methods to extract characteristic features of flows [5, 32]. However, for geophysical applications, existing fluid-dedicated methods do not use the underlying physical laws. Moreover, geophysical flows are quite well described by appropriate physical models. As a consequence in such contexts, physic-based approach can be very powerful for analyzing incomplete and noisy image data, in comparison to standard statistical methods. The inclusion of physical *a priori* leads to unusual advanced techniques for motion analysis.

We propose 3 different methods in this paper which are significantly different from previous works on motion analysis by satellite imagery. All methods estimate physical sound and time consistent motion fields retrieved at different atmospheric levels from image sequence.

- In the first method, we propose a mass conservation model for an atmosphere decomposed into a stack of layers. This model constitutes the physical background of a multi-layer dense estimator. In the perspective of adapting motion analysis to mesoscale, we propose in this method a two-stage decomposition estimation scheme. We propose to combine the ability of correlation and variational approaches and to enhance spatio-temporal consistency by using a simplified shallow water model [9].

- The second method proposed in this paper relies on an exact 3D physical model for pressure difference image observations retrieved at different atmospheric levels. This interacting layered model allows us to recover a vertical motion information [10].

- In the last method, we use the exact shallow-water formulation of the Navier-Stokes equations to control the motion evolution across the sequence. This is done through a variational approach derived from data assimilation principle which combines the *a priori* exact dynamic and the pressure difference observations obtained from satellite images [20].

The three methods rely on sparse pressure difference image observations derived from top of cloud images and classification maps provided by the EUMETSAT consortium, the European agency which supplies the METEOSAT satellite data.

2   Image observations

2.1   Layer decomposition

The layering of atmospheric flow in the troposphere is valid in the limit of horizontal scales much greater than the vertical scale height, thus roughly for horizontal scales greater or equal to 100 km. It is thus impossible to truly characterize a layered atmosphere with a local analysis performed in the vicinity of a pixel characterizing a kilometer order scale. Nevertheless, one can still decompose the 3D space into elements of variable thickness, where only sufficiently thin regions of such elements may really correspond to common layers. Analysis based on such a decomposition presents the main advantage of operating at different atmospheric pressure ranges and avoids the mix of heterogeneous observations.

For the definition of the K layers, we present the 3D space decomposition introduced in [9]. The k-th layer corresponds to the volume lying in between an upper surface s^{k+1} and a lower surface s^k. These surfaces s^k are defined by the height of top of clouds belonging to the k-th layer. They are thus defined only in areas where there exists clouds belonging to the k-th layer, and remains undefined elsewhere. The membership of top of clouds to the different layers is determined by cloud classification maps. Such classifications, which are based on thresholds of top of cloud pressure, are routinely provided by the EUMETSAT consortium. Such classifications which are based on thresholds of top of cloud pressure, are routinely provided by the EUMETSAT consortium, the European agency which supplies the METEOSAT satellite data, as illustrated in figure 1.
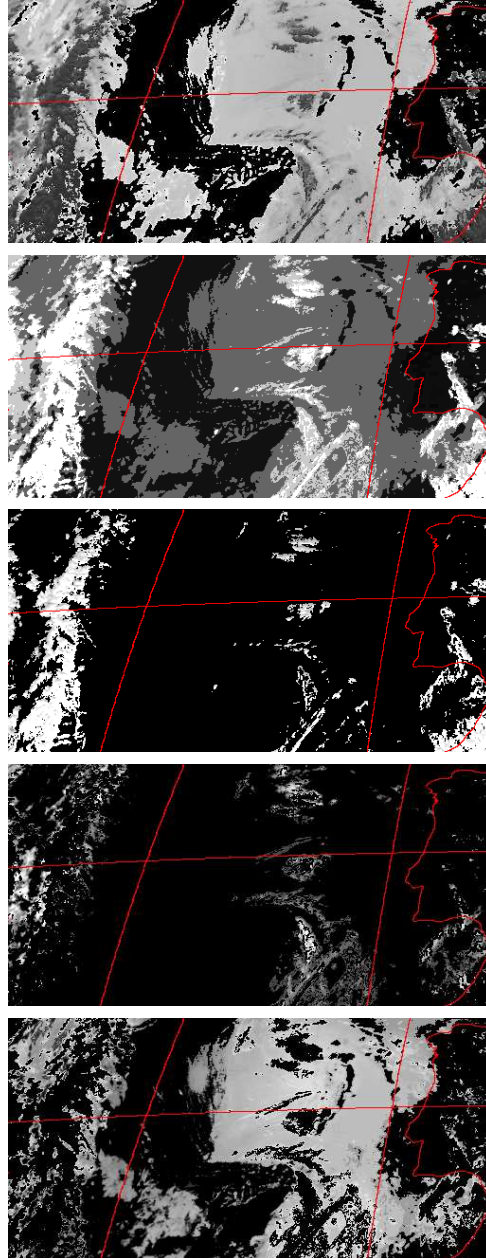
Figure 1: **Image observations**. *From top to bottom : cloud top pressure image; classification into low (in dark gray), medium (in light gray) and high (in white) clouds; pressure difference of the higher layer; pressure difference of the intermediate layer; pressure difference of the lower layer. Black regions correspond to missing observations and red lines represent costal contours, meridians and parallels (every 10°).*

2.2   Sparse pressure difference image observations

Top of cloud pressure images are also routinely provided by the EUMETSAT consortium. They are derived from a radiative transfer model using ancillary data obtained by analysis or short term forecasts. Multi-channel techniques enable the determination of the pressure at the top of semi-transparent clouds [24].

We denote by C^k the class corresponding to the k-th layer. Note that the top of cloud pressure image denoted by $p_\bigcup$ is composed of segments of top of cloud pressure functions $p(s^{k+1})$ related to the different layers. That is to say: $p_\bigcup = \{\bigcup_k p(s^{k+1}, \mathbf{s}); \ \mathbf{s} \in C^k\}$. Thus, pressure images of top of clouds are used to constitute sparse pressure maps of the layer upper boundaries $p(s^{k+1})$. As in satellite images, clouds lower boundaries are always occluded, we coarsely approximate the missing pressure observations $p(s^k)$ by an average pressure value $\overline{p}^k$ observed on top of clouds of the layer underneath. Finally, for layer $k \in [1, K]$, we define observations h^k_{obs} as pressure differences in hecto Pascal (hPa) units:

$$h^k_{obs} \begin{cases} = \overline{p}^k(\mathbf{s}) - p_\bigcup & if \quad \mathbf{s} \in C^k \\ = 0 & if \quad \mathbf{s} \in \bar{C}^k, \end{cases} \tag{1}$$

Resulting image observations are illustrated in figure 1.

3   Fine mesoscale estimation of 2D winds of a multi-layer model

3.1   Related work on optical-flow estimation

The problem of wind field recovery in an image sequence $I(x, y, t)$ consists in estimating the real three-dimensional atmospheric motion from observations in the projected image plane. This problem is a complex one, for which we have only access to projected information on clouds position and spectral signatures provided by satellite observation channels. Spatial horizontal coordinates (x, y) are denoted by $\mathbf{s}$. To avoid tackling the three-dimensional wind field $\mathbf{V}(\mathbf{s}, z, t)$ reconstruction problem, up to now all the developed wind field estimation methods rely on the assumption of inexistent vertical winds and consists to estimate an average horizontal wind.

3.1.1   Real projected wind fields and optical-flow

The apparent motion $\mathbf{v} = (u, v)$, perceived through image intensity variations, can be computed with the standard Optical Flow Constraint (OFC):

$$I_t(\mathbf{s}, t) + \mathbf{v} \cdot \boldsymbol{\nabla} I(\mathbf{s}, t) = 0. \tag{2}$$

For image sequences showing evolving atmospheric phenomena, the brightness consistency assumption does not allow to model temporal distortions of luminance patterns caused by 3D flow transportation. For transmittance imagery of fluid flows, the so called continuity equation :

$$\frac{1}{\rho}\frac{D\rho}{Dt} + \mathbf{\nabla}.\mathbf{V} = 0, \tag{3}$$

may be derived from the 3D mass conservation law, where ρ denotes a three-dimensional density function. In this case, an apparent motion $\mathbf{v}$ is redefined as a density-weighted average of the original three-dimensional horizontal velocity field. For the case of a null motion on the boundary planes, in [7], the author showed that the integration of Eq.3 leads to a 2D Integrated Continuity Equation (ICE):

$$\left(\int \rho dz\right)_t + \mathbf{v}.\mathbf{\nabla}\left(\int \rho dz\right) + \left(\int \rho dz\right)\mathrm{div}(\mathbf{v}) = 0, \tag{4}$$

Unlike the OFC, such models can compensates mass departures observed in the image plan by associating two-dimensional divergence to brightness variations. By time integration, an equivalent non-linear formulation can be recovered [5] :

$$\left(\int \rho dz\right)(\mathbf{s} + \mathbf{v}, t + 1)\exp\mathrm{div}(\mathbf{v}) - \left(\int \rho dz\right)(\mathbf{s}, t) = 0. \tag{5}$$

The image formation model for satellite infrared imagery is slightly different. In [5], the authors have directly assumed the unrealistic hypothesis that infrared pixel values I were proportional to density integrals : $I \propto \int \rho dz$. In [32], the authors proposed an inversely proportional approximation for infrared measurements : $I \propto (\int \rho dz)^{-1}$.

3.1.2 Regularization schemes and minimization issues

The previous formulations of Eq. 2, 4 and 5 can not be used alone, as they provide only one equation for two unknowns at each spatio-temporal locations $(\mathbf{s}, t)$. To deal with this problem, the most common assumption consists in enforcing spatial and temporal local coherence.

Disjoint local smoothing methods considers neighborhoods centered at pixel locations. An independent parametric field is locally estimated on each of these supports. In the the work of *Lucas and Kanade* [17], relying on the OFC equation, motion which is assumed to be locally constant is estimated using a standard linear least square approach. In meteorology, classical approaches are Euclidean correlation-based matchings, which corresponds to the OFC constraint associated to a locally constant field and a $\mathbf{L}^2$ norm [16, 24]. On the one hand, these methods are fast and are able to estimate large displacement of fine structures. On the other hand, they present the drawback to be sensitive to noise and inefficient in the case of weak intensity gradients. Moreover, estimation with these approaches is prone to erroneous spatial variability and results in the estimation of sparse and possibly incoherent vector fields.

Globalized smoothing schemes can be used to overcome the previous limitations. These methods model spatio-temporal dependencies on the complete image domain. Thus, dense velocity fields are estimated even in the case of noisy and low contrasted observations. More precisely, the motion estimation problem is defined as the global minimization of a energy function composed of two components :

$$J(\mathbf{v}, I) = J_d(\mathbf{v}, I) + \alpha J_r(\mathbf{v}). \tag{6}$$

The first component $J_d(\mathbf{v}, I)$ called the data term, expresses the constraint linking unknowns to observations while the second component $J_r(\mathbf{v})$, called the regularization term, enforces the solution to follow some smoothness properties. In the previous expression, $\alpha > 0$ denotes a parameter controlling the balance between the smoothness and the global adequacy to the observation model. In this framework, Horn and Schunck [14] first introduced a data term related to the OFC equation and a first-order regularization of the two spatial components u and v of velocity field $\mathbf{v}$. In the case of transmittance imagery of fluid flows, $I = \int \rho dz$, and using the previously defined ICE model (Eq.4) leads to the functional :

$$J_d(\mathbf{v}, I) = \int_{\Omega} \left(I_t(\mathbf{s}) + \mathbf{v}(\mathbf{s}) \cdot \boldsymbol{\nabla} I(\mathbf{s}) + I(\mathbf{s}) \mathrm{div}(\mathbf{v}(\mathbf{s})) \right)^2 d\mathbf{s}. \tag{7}$$

Moreover, it can be demonstrated that a first order regularization is not adapted as it favors the estimation of velocity fields with low divergence and low vorticity. A second order regularization on the vorticity and the divergence of the defined motion field can advantageously be consider as proposed in [26][5][31] :

$$J_r(\mathbf{v}) = \int_{\Omega} \| \boldsymbol{\nabla} curl \mathbf{v}(\mathbf{s}) \|^2 + \| \boldsymbol{\nabla} div \mathbf{v}(\mathbf{s}) \|^2 d\mathbf{s}. \tag{8}$$

Instead of relying on a $\boldsymbol{L}^2$ norm, robust penalty function ϕ_d may be introduced in the data term for attenuating the effect of observations deviating significantly from the ICE constraint [4]. Similarly, a robust penalty function ϕ_r can be used if one wants to handle implicitly the spatial discontinuities of the vorticity and divergence maps. In the image plan, these discontinuities are nevertheless difficult to relate to abrupt variations of clouds height . Moreover, layers clouds form unconnected regions which should interact during the motion estimation process.

OFC or ICE model rely on the assumption that the intensity function can be locally efficiently approximated by a linear function. Since the larger the displacement the more narrow the linearity domain, large displacements are difficult to recover directly. The multiresolution approach is a common way to overcome this limitation. However, since the multiresolution schemes estimates principal component displacements only at coarse resolutions where small photometric structures are rubbed out, this approach enables the characterization of large displacements of small structures only in the case when their motion are close enough to the principal component's one. This is often not the case for a multi-layered atmosphere.

3.2 Dense motion estimator dedicated to atmospheric layers

3.2.1 Dynamical model for layers

The ICE model relies on strong assumptions in the case of satellite infrared imagery. However, we demonstrated that this model is well suited for an image sequence of pressure difference measurements. Indedd, in the the isobaric coordinate system (x, y, p), the mass conservation equation reads :

$$\frac{\partial u}{\partial x} + \frac{\partial v}{\partial y} + \frac{\partial \omega}{\partial p} = 0, \tag{9}$$

where $\omega = \frac{dp}{dt}$ is the vertical wind in pressure coordinates. In order to perform the vertical integration of Eq. 9 in the pressure interval $[p(s^{k+1}), p(s^k)]$, we first fix the boundary conditions :

$$\begin{cases} \frac{\partial p(s^k)}{\partial t} + u(s^k)\frac{\partial p(s^k)}{\partial x} + v(s^k)\frac{\partial p(s^k)}{\partial y} & = & \omega(s^k) \\ \frac{\partial p(s^{k+1})}{\partial t} + u(s^{k+1})\frac{\partial p(s^{k+1})}{\partial x} + v(s^{k+1})\frac{\partial p(s^{k+1})}{\partial y} & = & \omega(s^{k+1}). \end{cases} \tag{10}$$

Such boundary conditions can be interpreted as the fact that boundary surfaces $p(s^k)$ and $p(s^{k+1})$ are deformed by vertical wind $\omega(s^k)$ and $\omega(s^{k+1})$. To achieve such a vertical integration in the pressure interval $[p(s^{k+1}), p(s^k)]$ varying with spatial coordinates, we employ the Leibnitz formula with the previous boundary conditions. This formula, which is valid for all integrable and derivable function $f(x, p)$ and for all interval $[a(x), b(x)]$ with boundaries varying with x, reads :

$$\int_{a(x)}^{b(x)} \frac{\partial f(x, p)}{\partial x} dp =$$
$$\frac{\partial}{\partial x}\left(\int_{a(x)}^{b(x)} f(x, p)dp\right) - f(x, b(x))\frac{\partial b(x)}{\partial x} + f(x, a(x))\frac{\partial a(x)}{\partial x}. \tag{11}$$

Thus, by vertical integration of the continuit equation of Eq. 9 in the pressure interval $[p(s^{k+1}), p(s^k)]$, the integrated mass conservation law reads :

$$\frac{\partial h^k}{\partial t} + \text{div}(h^k \mathbf{v}^k) = 0, \tag{12}$$

with

$$\begin{aligned} h^k & = & p(s^k) - p(s^{k+1}), \\ \mathbf{v}^k & = & (u^k, v^k) = \frac{1}{h^k}\int_{p(s^{k+1})}^{p(s^k)} \mathbf{v} dp, \end{aligned} \tag{13}$$

Note that as we are in the isobaric coordinate system, partial derivatives with respect to x, y and t are defined at constant pressure p. However, according to the previous section, pressure difference observations correspond to rough constant pressure interval. Therefore, such data fit the mass conservation model of Eq. 12 defined in the isobaric coordinate system.

3.2.2   Robust estimator for sparse observations

Relatively to the different layers, true pressure differences are sparsely observed only in the presence of clouds. A dense estimator dedicated to layer motion should consider simultaneously all cloudy regions belonging to a given layer while discarding the influence of other clouds. For the k-th layer, we previously remarked that outside the class 'C^k', the so defined pressure difference h_{obs}^k is not relevant of the k-th layer thickness. Thus, we propose to introduce in Eq.12 a masking operator on unreliable observations. We denote by $\mathbf{M}_{\mathbf{s} \in C^k}$ the operator which is identity if pixel belongs to the class, and which returns otherwise a fixed value out of the range taken by h_{obs}^k. Thus, applying this new masking operator in Eq.5, we obtain the robust data term $J_d(\mathbf{v}^k, h_{obs}^k)$:

$$\int_{\Omega} \phi_d \{ exp\mathrm{div}(\tilde{\mathbf{v}}(\mathbf{s}))([\tilde{h}^k(\mathbf{s}) \boldsymbol{\nabla} \mathrm{div}(\tilde{\mathbf{v}}(\mathbf{s})) + \boldsymbol{\nabla} \tilde{h}^k(\mathbf{s})]^T \breve{\mathbf{v}}^k(\mathbf{s}) + \tilde{h}^k(\mathbf{s})) - \mathbf{M}_{\mathbf{s} \in C^k}(h_{obs}^k(\mathbf{s})) \} d\mathbf{s}, \qquad (14)$$

where $\mathbf{v}^k = \tilde{\mathbf{v}} + \breve{\mathbf{v}}^k$ corresponds to the density-weighted average horizontal wind related to the k-th layer and where $\tilde{h}^k$ is the image observations h_{obs}^k compensated by the displacement field $\tilde{\mathbf{v}}$. The div-curl regularization term (Eq.8) is conserved. The masking procedure together with the use of robust penalty function on the data term allows to discard implicitly the erroneous observation from the estimation process. It is important to outline that, for the k-th layer, the method provides dense motion fields and areas outside class 'C^k' correspond to an interpolated wind field. Nevertheless, let us point out that in the case of very sparse observations and large displacements, robust estimation becomes unstable and may lead to erroneous minima. Such limitations will be overcome in the following.

3.3   A two level decomposition for mesoscale motion estimation

In order to enhance the estimation accuracy, a collection of correlation-based vectors $\mathbf{v}_c^k$ is introduced as sparse constraints in a differential estimation scheme for the recovery of a dense displacement field. Contrary to the classical multiresolution approach, this new technique enables to deal with the large displacements of small structures as it relies on a unique representation of the full resolution image. Moreover, in order to preserve spatio-temporal consistency of displacement estimates, we propose to incorporate in the estimation scheme an *a priori* physical knowledge on fluid dynamical evolution. A

dense displacement field $\bar{\mathbf{v}}_p^k$ is predicted by time integration of a simplified Navier-Stokes dynamical model. The propagated field is then introduced in the estimation process as a spatio-temporal regularizer. Keeping notations of section 3.1.2, a new functional is defined for the estimation of variable $\mathbf{v}^k = \bar{\mathbf{v}}^k + \check{\mathbf{v}}^k$

$$J(\mathbf{v}^k) = J_d(\bar{\mathbf{v}}^k + \check{\mathbf{v}}^k, h^k) + \alpha J_r(\bar{\mathbf{v}}^k + \check{\mathbf{v}}^k) + \gamma J_c(\bar{\mathbf{v}}^k, \mathbf{v}_c) + \beta J_p(\bar{\mathbf{v}}^k, \bar{\mathbf{v}}_p^k), \tag{15}$$

where $J_c(.)$, $J_p(.)$ are energy functions respectively constraining large scale displacements $\bar{\mathbf{v}}^k$ to be close to a sparse correlation-based vector field $\mathbf{v}_c$ and to be consistent with a physically sound large scale prediction $\bar{\mathbf{v}}_p^k$ relying on Navier-Stokes equations. In the previous expression, γ and β denote weighting factors. Functionals $J_c(.)$ and $J_p(.)$ will be further detailed in the following.

The displacement field $\mathbf{v}^k$ is decomposed into a large displacement field $\bar{\mathbf{v}}^k$ and an additive small displacement field $\check{\mathbf{v}}^k$. The optimization problem is conducted sequentially. Here, an analogous version of the alternate multigrid minimization scheme proposed in [5] has been implemented.

Note that in the case $\alpha, \beta, \gamma \gg 1$, the energy minimization leads to a large displacement field which can be seen as a physically sound spatio-temporal interpolation of the correlation-based vectors.

3.3.1 Variational approach for a correlation/optical-flow collaboration

In order to obtain a dense estimation of displacements fitting a sparse correlation-based displacement field, we define a functional where the ith correlation-based vector $\mathbf{v}_c^i = (u^i, v^i)$ located at the point $\mathbf{s}^i = (x^i, y^i)$ influences his neighborhood according to a shifted bi-dimensional Gaussian law $\mathcal{N}^i(\mathbf{s}^i - \mathbf{s})$ of variance σ related to the correlation window influence

$$J_c(\bar{\mathbf{v}}^k, \mathbf{v}_c^k) = \int_\Omega \mathbf{M}_{\mathbf{s} \in C^k} \left(\sum_{i=1}^K g^i \mathcal{N}^i(\mathbf{s}^i - \mathbf{s}) \phi_c\{\mathbf{v}_c^i - \bar{\mathbf{v}}^k(\mathbf{s})\} \right) d\mathbf{s}, \tag{16}$$

where ϕ_c is a robust penalty function similar to the one attached to the data term. In the previous expression, g^i denote confidence factors. We choose, to define them according to the dissimilarity function. The masking operator $\mathbf{M}_{\mathbf{s} \in C^k}()$ was introduced as the correlation/optical-flow collaboration is not possible in regions with no image observations.

3.3.2 Spatio-temporal regularization

The functional $J_p(.)$ aims at constraining a motion field to be consistent with a physically predicted wind field. We simply define this functional as a quadratic distance between the estimate field $\mathbf{v}^k$ and the dense propagated field $\bar{\mathbf{v}}_p^k$:

$$J_p(\bar{\mathbf{v}}^k, \bar{\mathbf{v}}_p^k) = \int_\Omega \| \bar{\mathbf{v}}_p^k(\mathbf{s}) - \bar{\mathbf{v}}^k(\mathbf{s}) \|^2 d\mathbf{s}. \tag{17}$$

This approach constitutes an alternative to the spatio-temporal regularizer defined in [29] and is to some extend similar to the temporal constrain introduced in [21]. Our propagation model includes a bi-dimensional divergence component which is equal to zero only for incompressible bi-dimensional flows. As it is detailed below, our approach extends [21] to the spatio-temporal smoothing of the full velocity field in the case of three-dimensional geophysical flows driven by a shallow-water evolution law. Dynamical models describing wind field evolution are needed here for the prediction at time $t+1$ of a sound field $\bar{\mathbf{v}}_p^k$ using a filtered version $\bar{\mathbf{v}}^k$ of a previous motion estimation $\mathbf{v}^k$ performed for the k-th layer between time $t-1$ and t. As atmosphere evolution is governed by fluid flows laws, we rely on Navier-Stokes equations in order to derive simplified dynamical models adapted to short time propagation of layer large mesoscale motions.

At the upper range of mesoscale, friction components and terms depending on Earth curvature can be neglected [9] [12]. Let us denote by (u,v) the horizontal wind components. Using the shallow-water approximation (horizontal scale much greater than vertical scale), the horizontal momentum equations for atmospheric motion read :

$$\begin{cases} \frac{du}{dt} + \frac{p_x}{\rho_0} - vf^\phi & = & 0 \\ \frac{dv}{dt} + \frac{p_y}{\rho_0} + uf^\phi & = & 0 \end{cases} \tag{18}$$

where ρ_0 and f^ϕ denote the local mean density and the coriolis factor depending on latitude ϕ. In order to make valid the layering assumption (horizontal scales of order of 100 km) while extracting information on a pixel grid associated to high resolution images, we filter Navier-Stokes Eq. 18 with a Gaussian kernel function K_{Δ_x} of standard deviation equal to $\Delta_x = 100\delta_p^{-1}$ where δ_p^{-1} denote the image pixel resolution in kilometers. The resulting filtered momentum equations under the shallow-water approximation read :

$$\begin{cases} \frac{\partial \bar{u}}{\partial t} + \bar{u}\frac{\partial \bar{u}}{\partial x} + \bar{v}\frac{\partial \bar{u}}{\partial y} + \omega\frac{\partial \bar{u}}{\partial p} + \frac{\bar{p}_y}{\rho_0} - \bar{v}f^\phi & = & \mathcal{T}_{\bar{u}} \\ \frac{\partial \bar{u}}{\partial t} + \bar{u}\frac{\partial \bar{v}}{\partial x} + \bar{v}\frac{\partial \bar{v}}{\partial y} + \omega\frac{\partial \bar{v}}{\partial p} + \frac{\bar{p}_y}{\rho_0} + \bar{u}f^\phi & = & \mathcal{T}_{\bar{v}} \end{cases} \tag{19}$$

where, $(\bar{u},\bar{v})$, $\bar{p}$ and $\mathcal{T} = (\mathcal{T}_{\bar{u}}, \mathcal{T}_{\bar{v}})^\top$ are the filtered horizontal components of motion, the filtered pressure and the turbulent viscosity dissipation forces produced at sub-grid scales [8]. In order to simplify the previous horizontal equations, we assumed filtered horizontal motion components to be homogenous within the layer. In other words, we neglect their vertical derivatives and consider that filtered horizontal winds $\bar{\mathbf{v}}^k$ which have been vertically averaged are equal to filtered horizontal winds on layer upper surfaces

$\mathbf{s}^{k+1}$. Using such an assumption, Eq.19 yields to :

$$\bar{\mathbf{v}}_t^k + \boldsymbol{\nabla}(\bar{\mathbf{v}}^k)\bar{\mathbf{v}}^k - \rho_0^{-1}\nabla\bar{p}(s^{k+1}) + \begin{bmatrix} 0 & -1 \\ 1 & 0 \end{bmatrix} f^\phi \bar{\mathbf{v}}^k = \mathcal{T} \tag{20}$$

with the notations $\boldsymbol{\nabla}(\bar{\mathbf{v}}^{\mathbf{k}}) = (\boldsymbol{\nabla}\bar{u}^k, \boldsymbol{\nabla}\bar{v}^k)^\top$. Let us denote the vorticity by $\bar{\zeta}^k = \mathrm{curl}(\bar{\mathbf{v}}^k)$ and the divergence by $\bar{D}^k = \mathrm{div}(\bar{\mathbf{v}}^k)$. The previous system may be expressed in its vorticity-divergence form :

$$\begin{cases} \bar{\zeta}_t^k + \bar{\mathbf{v}}^k \cdot \nabla\bar{\zeta}^k + (\bar{\zeta}^k + f^\phi)\bar{D}^k = \mathrm{curl}(\mathcal{T}) \\ \bar{D}_t^k + \bar{\mathbf{v}}^k \cdot \nabla\bar{D}^k + (\bar{D}^k)^2 - 2|J| - \rho_0^{-1}\Delta\bar{p}(s^{k+1}) + f^\phi\bar{\zeta}^k = \mathrm{div}(\mathcal{T}) \end{cases} \tag{21}$$

where $|J|$ is the determinant of the Jacobian matrix of variables $(\bar{u}^k, \bar{v}^k)$.

The induced turbulent dissipation can be approached by sub-grid models proposed in large eddy simulation literature [22]. The simplest one is the well known Smagorinsky sub-grid model which is in agreement with Kolmogorov "K41" theory [25]. For a vorticity based large eddy simulation formulation, we may rely on similar enstrophy-based subgrid models based on Taylors vorticity transfer and dissipation by small scales theory [28]. Consequently, sub-grid turbulent dissipation term in the curl transport equation may be modeled by the enstrophy-based sub-grid model proposed in [19]. Such a model reads :

$$\mathrm{curl}(\mathcal{T}) = (C\Delta_x)^2 |\bar{\zeta}^k|\Delta\bar{\zeta}^k, \tag{22}$$

with the universal value of C equal to 0.17.

In the momentum conservation formulations of Eq. 20 and Eq. 21, dynamical models predict the evolution of velocity fields $(\bar{u}^k, \bar{v}^k)$ and of divergence-vorticity fields $(\bar{\zeta}^k, \bar{D}^k)$. In both models, one of the major difficulties is induced by the dependence to pressure variable $\bar{p}(s^{k+1})$ which is known only at given temporal locations and only for cloudy regions corresponding to the k-th layer. However, in opposition to the classical formulation, the vorticity-divergence equations provide a dynamical model for which the vorticity evolution is independent of the pressure variable. Moreover, as at the large scales divergence can be considered weak almost everywhere, we propose to simplify the divergence dynamical model by neglecting the pressure diffusion term and by assuming that the vorticity sub-grid model of Eq. 22 can also apply for the divergence evolution. Finally, the simplified filtered vorticity-divergence model reads :

$$\begin{cases} \bar{\zeta}_t^k + \bar{\mathbf{v}}^k \cdot \nabla\bar{\zeta}^k + (\bar{\zeta}^k + f^\phi)\bar{D}^k = (C\Delta_x)^2|\bar{\zeta}^k|\Delta\bar{\zeta}^k \\ \bar{D}_t^k + \bar{\mathbf{v}}^k \cdot \nabla\bar{D}^k + (\bar{D}^k)^2 - 2|J| + f^\phi\bar{\zeta}^k = (C\Delta_x)^2|\bar{\zeta}^k|\Delta\bar{D}^k \end{cases} . \tag{23}$$

The curl and divergence completely determine the underlying 2D velocity field and the current velocity estimate can be recovered from these quantities up to a laminar flow. Indeed, denoting the orthogonal gradient by $\boldsymbol{\nabla}^{\perp} = (-\partial/\partial y, \partial/\partial x)^{\top}$, the Helmholtz decomposition of the field into a sum of gradients of two potential functions is expressed as

$$\bar{\mathbf{v}}^k = \boldsymbol{\nabla}^{\perp}\Psi + \boldsymbol{\nabla}\Phi + \bar{\mathbf{v}}_{har}^k, \tag{24}$$

where $\bar{\mathbf{v}}_{har}^k$ is a harmonic transportation part ($div\bar{\mathbf{v}}_{har}^k = \mathrm{curl}\bar{\mathbf{v}}_{har}^k = 0$) of the field $\bar{\mathbf{v}}^k$ and where the stream function Ψ and the velocity potential Φ correspond to the solenoidal and the irrotational part of the field. The latter are linked to divergence and vorticity through two Poisson equations. Expressing the solution of both equations as a convolution product with the 2D Green kernel G associated with the Laplacian operator: $\Psi = G * \zeta, \quad \Phi = G * D$, the whole velocity field can be recovered with the equation :

$$\bar{\mathbf{v}}^k = \boldsymbol{\nabla}^{\perp}(G * \bar{\zeta}^k) + \boldsymbol{\nabla}(G * \bar{D}^k) + \bar{\mathbf{v}}_{har}^k, \tag{25}$$

which can be efficiently solved in the Fourier domain. The harmonic transportation component $\bar{\mathbf{v}}_{har}^k$ is recovered by substracting to the field $\bar{\mathbf{v}}^k$ its solenoidal and irrotationnal parts.

Let us sum up this prediction process. The vorticity and the divergence fields are developed in time in between consecutive image frame using a discretized form of Eq. 23 and time increments δt. After each time increment, assuming $\bar{\mathbf{v}}_{har}^k$ constant within each frame interval, Eq. 25 is used to update the velocity $\bar{\mathbf{v}}^k$ needed by Eq. 23, with the current vorticity and divergence estimates.

To avoid instability, a semi-implicit time discretization scheme is used to integrate forward Eq. 23. Classical centered finite difference schemes are used for the curl and divergence discretization. Geometrical deformations due to slant view effects are neglected for geostationary satellite observations at tropical and temperate latitudes in order to perform spatial discretization using directly the pixel grid. Let us note that this equation system describes the dynamics of physical quantities expressed in standard units. Thus, a dimension factor appears in front of the coriolis factor when this equation system is discretized on a pixel grid with velocity expressed in pixel per frame.

To solve the linear system associated with the semi-implicit discretization scheme, the matrix has been constrained to be diagonally dominant, which is a sufficient condition for a well-conditioned inversion

From time index $t = 1$ to the last image index :

- $p_\cup(t)$ and $p_\cup(t+1) \leftarrow$ read pressure images

- $\{(h_\rho^k(t), h_\rho^k(t+1))\} \leftarrow$ recovery of $2K$ transmittance images

- $\mathbf{v}_c(t) \quad \leftarrow$ extraction of a correlation-based vector field

- For layer index $k = 1$ to K :

  - $\bar{\mathbf{v}}^k(t) = 0, \check{\mathbf{v}}^k(t) = 0, \tilde{h}_\rho^k(t) = h_\rho^k(t+1)$

  - **Large scale** motion estimation

    * Introduction of functionals $J_p(.)$ and $J_c(.)$

    * If t=0, $\gamma = 0$

    * Until convergence (alternate multigrid optimization) :

      · $\bar{\mathbf{v}}^k(t) \leftarrow \text{GS(Eq. 15)}^1$ w.r.t. $\bar{\mathbf{v}}^k(t)$

      · $\zeta_{\mathbf{v}} \leftarrow \text{GS(Eq. 15)}$ w.r.t. $\zeta_{\mathbf{v}}$

      · $D_{\mathbf{v}} \leftarrow \text{GS(Eq. 15)}$ w.r.t. $D_{\mathbf{v}}$

      · $\tilde{h}_\rho^k(t) \leftarrow$ compensate image $h_\rho^k(t+1)$ with $\bar{\mathbf{v}}^k(t)$

  - **Fine scale** motion increment estimation

    * Removal of functionals $J_p(.)$ and $J_c(.)$

    * Until convergence (alternate multigrid optimization) :

      · $\check{\mathbf{v}}^k(t) \leftarrow \text{GS(Eq. 15)}$ w.r.t. $\check{\mathbf{v}}^k(t)$

      · $\zeta_{\mathbf{v}} \leftarrow \text{GS(Eq. 15)}$ w.r.t. $\zeta_{\mathbf{v}}$

      · $D_{\mathbf{v}} \leftarrow \text{GS(Eq. 15)}$ w.r.t. $D_{\mathbf{v}}$

      · $\mathbf{v}^k(t) \leftarrow \bar{\mathbf{v}}^k(t) + \check{\mathbf{v}}^k(t)$

      · $\tilde{h}_\rho^k(t) \leftarrow$ compensate image $h_\rho^k(t+1)$ with $\mathbf{v}^k(t)$

  - $\bar{\mathbf{v}}_p^k(t+1) \leftarrow$ **propagation** of $\bar{\mathbf{v}}^k(t)$ via Eq.23 and Eq.25

---

[1] "GS(Eq. 15)" denotes one Gauss-Seidel iteration used for the minimization of Eq. 15. Note that in this algorithm the robust parameter estimation steps have been omitted for clarity.

Figure 2: *Global flowchart for 2D layered atmospheric motion estimation.*

problem. This condition reads $1/\delta t \geq \max_s(|\bar{u}^k| + |\bar{v}^k| - |\bar{D}^k|)$.

Finally, the dynamical model time integration is done independently for each layer. This procedure results in a predicted average horizontal wind field $\bar{\mathbf{v}}_p^k$ related to each layer.

The complete algorithm for atmospheric motion estimation is summarized in figure 2.

3.4   Experimental evaluation

For an exhaustive evaluation, we first propose to rely on a simulated flow. A Direct Numerical Simulation (DNS) of a 2D, incompressible, and highly turbulent flow has been used to generated an image sequence depicting the motion of a continuous scalar field. The sequence of scalar images of 256 by 256 pixels together with the true vector fields generated by the DNS were provided by the laboratory of fluid mechanics of *Cemagref (center of Rennes, France)*. The thickness conservation model reduces in this 2D case to the classical OFC data model. Note that as divergence vanishes, the spatio-temporal regularization constrains only vorticity to be coherent in time.

In order to experiment our method with correlation-based vectors with different noise level, the correlation-based vectors have been substituted by DNS vectors contaminated by an additive Gaussian noise. As correlation techniques only operate on contrasted regions, vector constraints were attached to regions with sufficient gradient. To be realistic with correlation measurements, DNS vectors have been sub-sampled in those regions. DNS velocity vectors which have been selected as non-noisy correlation measurements are presented in fig.3. They are superimposed to the scalar image.   Based on the
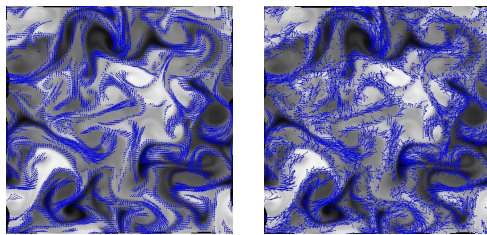

Figure 3:   ***Velocity constraints and fluid imagery for a bi-dimensional flow.*** *Left: velocity vectors provided by the DNS which have been selected as constraints are superimposed on the image. Right: Gaussian noise $\mathcal{N}(0, 1)$ has been added to these vectors.*
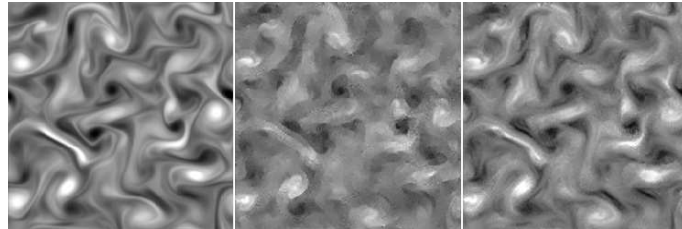
Figure 4: ***Comparison on the image domain of multiresolution and collaborative schemes in the case of a bi-dimensional flow.*** *Left: vorticity provided by the DNS. Center: vorticity estimation by the fluid flow dedicated multiresolution approach of [5].Right: vorticity estimation after the second level of the collaborative scheme.*

non-noisy correlation constraints defined previously, we first compare our two-level collaborative scheme to the fluid flow dedicated multiresolution approach described in [5]. In Fig.4, it clearly appears that the multiresolution approach hardly estimates fine turbulent structure while the collaborative method manages to recover most of the vorticity field structures. Indeed, in scalar imagery, low contrast regions correspond to high vorticity areas. Thus, the multiresolution technique suffers from a lack of information in those crucial regions. And, incorporating motion constraints in contrast areas around vortices reduces the degree of freedom of the solution and thus, considerably enhances the estimated motion field. In
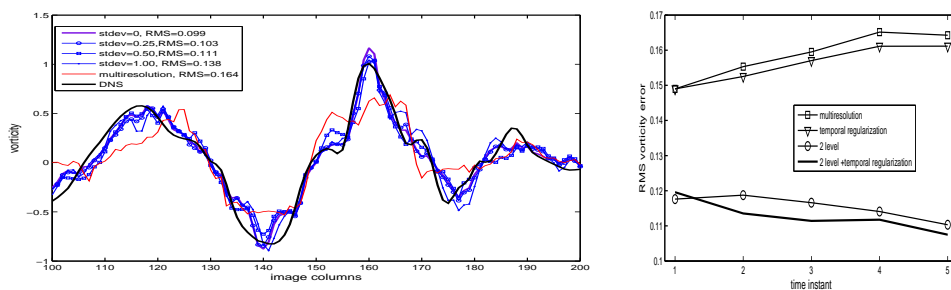

Figure 5: ***Influence of noise and spatio-temporal regularization.*** *Left: for increasing noise, vorticity estimates on a slice of the image and global RMS vorticity error in comparison to the multiresolution approach. Right: RMS vorticity errors on five consecutive estimations for the multiresolution approach, the collaborative scheme constrained by noisy correlation vectors combined or not with spatio-temporal regularization.*

order to evaluate the robustness of the collaborative method to inaccurate constraints, Gaussian noise of zero mean and increasing variance has been added to the true velocity vectors provided by the DNS. Constraint examples are displayed in Fig.3. In Fig.5, we can visually inspect the influence of noise on the estimated solution for a particular horizontal slice of the image and for the global image domain by referring to RMS errors on vorticity values. It clearly appears that, even in presence of noise, motion estimation is better achieved by our collaborative scheme than by a classical multiresolution approach. Spatio-temporal regularization benefits which are assessed for both, multiresolution and collaborative methods, are shown in Fig.5.

We then turned to qualitative comparisons on a real meteorological image sequence. The benchmark data was composed by a sequence of 18 Meteosat Second Generation (MSG) images, showing thermal infrared radiation at a wavelength of 10.8 mm. The 512 x 512 pixel images cover an area over the North-Atlantic Ocean, off the Iberian peninsula, during part of one day (5-June-2004), at a rate of one image every 15 minutes. The spatial resolution is 3 kilometers at the center of the whole Earth image disk. Clouds from a cloud-classification product derived from MSG images by the operational centre EUMETSAT, are used to segment images into 3 broad layers, at low, intermediate and high altitude. This 3 layers decomposition is imposed by the EUMETSAT classification. Applying the methodology previously described, pressure difference images were derived for these 3 layers.

Trajectories reconstructed by a Runge-Kutta integration method [5] from the estimated wind fields provide a practical visualization tool to assess the quality of the estimation in time and space.
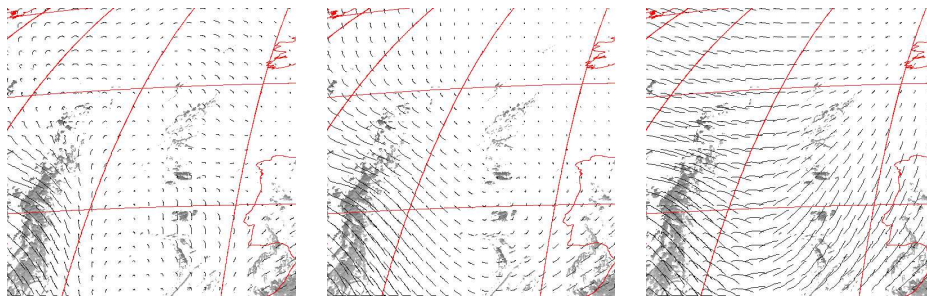

Figure 6: ***Collaborative approach and spatio-temporal regularization influence*** *on the estimation of wind field for the highest layer. Trajectories reconstruction for an estimation scheme without (left) and with (center) spatio-temporal regularization. Trajectories reconstruction for the two-level collaborative estimation scheme with spatio-temporal regularization (right).*
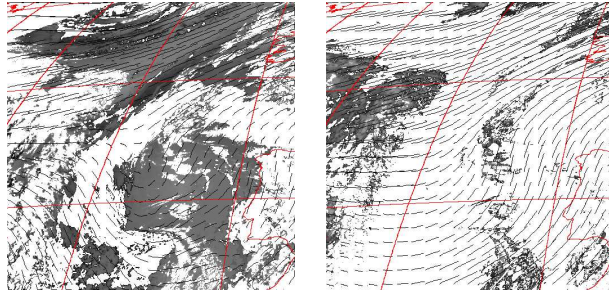
Figure 7: ***Middle layer and lower layer trajectories for a two-level collaborative estimation scheme using spatio-temporal regularization.*** *The trajectories correspond to the low (right), and to the medium (left) layer motions.*

The enhancements brought by the collaborative estimation scheme for the recovery of a wind field related to the highest layer is shown in Fig.6. It can be noticed in this comparative figure that the introduction of spatio-temporal constraints smooths trajectory discontinuities and, together with the introduction of correlation constraints, propagate motion in regions where observations are missing. Using the collaborative framework and the spatio-temporal regularizer, trajectories related to the other layers are presented in Fig.7. In the middle of the image, one can notice the estimation of two perpendicular motions : the upward motion related to sparse clouds of the intermediate layer has been accurately recovered above an underneath stratus moving downward.

4 Fine mesoscale estimation of 3D winds of a multi-layer model

In this section, we revisit the integrated continuity equation expressed in a pressure coordinate system in the presence of vertical winds and then derive a 3D dynamical model for a stack of interacting layers fitting sparse pressure difference observations.

4.1 Revisiting the integrated Continuity Equation for 3D winds

Interesting models for 3D compressible atmospheric motion observed through image sequences may be derived by integrating the 3D continuity equation expressed in the isobaric coordinate system (x, y, p). In comparison to standard altimetric coordinates, isobaric coordinates are advantageous : they enable to handle in a simple manner the compressibility of atmospheric flows while dealing directly with pressure

quantities, which will be used as observations in this paper. In this coordinate system, the pressure function p acts as a vertical coordinate. By using the previously defined pressure difference function h^k and the pressure-average horizontal wind field $\mathbf{v}^k$, we now demonstrate that the vertical integration of Eq.9 in the altimetric interval $[s^k, s^{k+1}]$ yields under certain conditions to the following 3D-ICE model:

$$g\rho(s^k)\mathrm{w}(s^k) - g\rho(s^{k+1})\mathrm{w}(s^{k+1}) = \frac{dh^k}{dt} + h^k\mathrm{div}(\mathbf{v}^k), \tag{26}$$

where g and w denote the gravity constant and the vertical wind in the standard altimetric coordinate system (x, y, z).

Indeed, for compressible fluids, according to the Leibnitz formula (Eq. 11), integrating the continuity equation (Eq. 9) in the (x, y, p) coordinates system in the varying pressure interval $[p(s^{k+1}), p(s^k)]$ yields to :

$$[\omega]_{s^k}^{s^{k+1}} = \mathrm{div}\Big|_p \int_{p(s^{k+1})}^{p(s^k)} \mathbf{v}dp - \mathbf{v}(s^k).\nabla_{xy}(p(s^k))\Big|_{s^k} + \mathbf{v}(s^{k+1}).\nabla_{xy}(p(s^{k+1}))\Big|_{s^{k+1}} \tag{27}$$

Moreover, expanding ω in the (x, y, z) coordinates system and using the hydrostatic assumption ($\frac{\partial p}{\partial z} = -\rho g$) yields to

$$\omega = \frac{dp}{dt} = \frac{\partial p}{\partial t} + \mathbf{v} \cdot \nabla_{xy}(p) - \mathrm{w}\rho g, \tag{28}$$

where w is the vertical velocity in z coordinates and where we have introduced the density functions ρ and the gravity constant g. Assuming that the surface s^k is flat in the vicinity of a pixel, by merging Eq. 27 and Eq. 28, we obtain

$$g[\rho\mathrm{w}]_{s^{k+1}}^{s^k} + \frac{\partial(p(s^{k+1}) - p(s^k))}{\partial t}\Big|_{I_s} \simeq \mathrm{div}\Big|_p \int_{p(s^{k+1})}^{p(s^k)} \mathbf{v}dp \tag{29}$$

where we have denoted by I_s the altimetric interval between surfaces s^k and s^{k+1}. Using notations of Eq. 13 while considering the reasonable approximation $\mathrm{div}(\mathbf{v}^k)\Big|_p \simeq \mathrm{div}(\mathbf{v}^k)\Big|_{I_s}$, we can then rewrite Eq. 29 as

$$g\rho(s^k)\mathrm{w}(s^k) - g\rho(s^{k+1})\mathrm{w}(s^{k+1}) \simeq$$
$$\left.\frac{\partial h^k}{\partial t}\right|_{I_s} + \mathbf{v}^k \cdot \nabla_{xy}(h^k)\Big|_{I_s} + h^k \mathrm{div}(\mathbf{v}^k)\Big|_{I_s}, \tag{30}$$

Simplifying notations of operators defined for the altimetric interval I_s, we obtain Eq. 26, which consitutes a proper image-adapted model for observations h^k related to a layer defined in the interval I_s.

Note that this model appears to be a generalization of the so called *kinematic method* applied in meteorology for the recovery of vertical motion [12]. Indeed, by neglecting the first term on the right hand side of Eq.26, vertical motion can be expressed as :

$$\mathrm{w}(s^{k+1}) = \frac{\rho(s^k)\mathrm{w}(s^k)}{\rho(s^{k+1})} - \frac{h^k}{g\rho(s^{k+1})}\mathrm{div}(\mathbf{v}^k), \tag{31}$$

which corresponds exactly to the *kinematic* estimate. Note also that the ICE model (Eq.12) can be recovered when vertical motion is neglected and for an atmosphere in hydrostatic equilibrium ($\delta p = -g \int \rho dz$). On the right side of the 3D-ICE, vertical motion w appears only on the integration boundaries, while on the left side, pressure-average horizontal motion $\mathbf{v}^k$ appears within a standard optical flow expression compensated by a divergence correcting term. Thus, for pressure difference observations on layer boundaries, the 3D-ICE constitutes a possible 3D estimation model.

4.1.1 Layer interacting model

Eq.26 is thus valid for image observations h^k related to the k-th layer on the spatial sub-domain C^k:

$$\frac{d(h^k)}{dt} + h^k \nabla \cdot \mathbf{v}^k = g(\rho^k \mathrm{w}^k - \rho^{k+1} \mathrm{w}^{k+1}), \tag{32}$$

where for clarity we have simplified notations $\rho(s^k)$ and $w(s^k)$ into ρ^k and w^k. Density maps ρ^k are fixed to a mean density value, which is computed according to the mean pressures $\overline{p}^k$ using the approximation : $\rho^k \approx p_0/(RT_0)(\overline{p}^k/p_0)^{(\gamma R)/g+1}$, where p_0, T_0, γ and R denote physical constants [12].

Integrating in time differential equation 32 along the horizontal trajectories and applying the variation of the constant tecnhique for the second member, we obtain a time-integrated form :
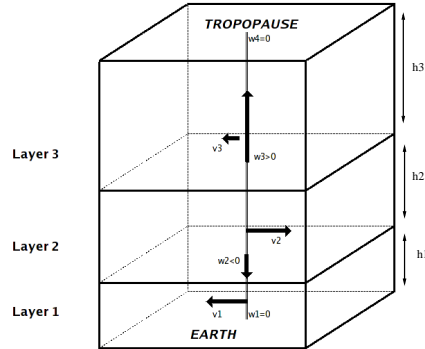
Figure 8: Scheme of three interacting layers defined at a given pixel location. The set of unknowns associated to the corresponding 3D-ICE model is $\{\mathbf{v}^1, w^2, \mathbf{v}^2, w^3, \mathbf{v}^3\}$. For the enhancement of the visual representation, pressure difference h^k have been identified here to altimetric heights.

$$\tilde{h}^k e^{\mathrm{div}\mathbf{v}^k} - h^k = g\Delta t \frac{\rho^k \mathrm{w}^k - \rho^{k+1}\mathrm{w}^{k+1}}{\mathrm{div}\mathbf{v}^k}(e^{\mathrm{div}\mathbf{v}^k} - 1), \tag{33}$$

where the motion-compensated image $h^k(\mathbf{s}+\mathbf{v}^k, t+\Delta t)$ has been denoted for convenience by $\tilde{h}^k$ and where Δt denotes the time interval expressed in seconds between two consecutive images.

For the lowest layer, the Earth boundary condition implies : $\mathrm{w}^1 = 0$. Let K denote the index of the highest layer. Another boundary conditions may be given for the highest layer by the reasonable assumption that vertical wind can be neglected at the tropopause which acts like a cover : $\mathrm{w}^{K+1} = 0$. Thus, as the vertical wind present on the upper bound of the k-th layer is identical to the one present on the lower bound of the $(k+1)$-th layer, we have the following two sets of unknowns : $\{\mathbf{v}^k : k \in [1, K]\}$ and $\{\mathrm{w}^k : k \in [2, K]\}$. The vertical wind unknowns act as variables materializing horizontal wind interactions between adjacent layers. Fig.8 schematizes an example of three interacting layers associated to a set of unknowns, according to the 3D-ICE model.

4.2   3D wind estimation

4.2.1   Dedicated robust estimator

Since outside the class C^k, h_{obs}^k defined in Eq.1 is not relevant of the k-th layer, we introduce a masking operator to remove unreliable observations by saturation of a robust penalty function ϕ_d. More explicitly, we denote by $\mathbb{I}_{C^k}$ the operator which is identity if pixel belong to the class, and which returns a fixed value out of the range taken by h_{obs}^k otherwise. Thus, applying this new masking operator in Eq.33, we obtain for the k-th layer the robust data term $J_d(\mathbf{v}^k, \mathrm{w}^k, \mathrm{w}^{k+1}, h_{obs}^k) =$

$$
\int_\Omega \phi_d\big[\tilde{h}_{obs}^k(\mathbf{s})\exp\{\mathrm{div}\mathbf{v}^k(\mathbf{s})\} - \mathbb{I}_{C^k}(h_{obs}^k(\mathbf{s}))
$$
$$
+g\Delta t\frac{\rho^k\mathrm{w}^k(\mathbf{s}) - \rho^{k+1}\mathrm{w}^{k+1}(\mathbf{s})}{\mathrm{div}\mathbf{v}^k(\mathbf{s})}(1 - \exp\{\mathrm{div}\mathbf{v}^k(\mathbf{s})\})\big]d\mathbf{s}. \tag{34}
$$

A second order div-curl regularizer has been chosen to constrain spatial smoothness of horizontal wind fields. The latter was combined with a first order regularizer enforcing regions of homogeneous vertical winds. Note that we have restricted the regularizer for vertical wind to be a first order one, as 3D divergence and 3D vorticity vectors are inaccessible in a layered model. The regularization term for the k-th layer has been thus defined as $J_r(\mathbf{v}^k, \mathrm{w}^k) =$

$$
\int_\Omega \alpha(\parallel \nabla curl\mathbf{v}^k(\mathbf{s})\parallel^2 + \parallel \nabla\mathrm{div}\mathbf{v}^k(\mathbf{s})\parallel^2) + \beta\parallel \nabla\mathrm{w}^k(\mathbf{s})\parallel^2 d\mathbf{s}, \tag{35}
$$

where $\beta > 0$ denotes a positive parameter. A Leclerc M-estimator has been chosen for ϕ_d for its advantageous minimization properties [11]. The masking procedure together with the use of this robust penalty function on the data term allows discarding implicitly the erroneous observations from the estimation process. It is important to outline that, for the k-th layer, the method provides estimates on all point s of the image domain Ω. Areas outside the cloud class C^k correspond to 3D interpolated wind fields.

4.2.2   Large horizontal displacements

One major problem with the differential formulation of Eq.32 is the estimation of large displacements. However, on the opposite of the integrated form of Eq.33 which is valid for high amplitude displacements, this formulation presents the advantage to be linear. A standard approach for tackling the non-linear

data term consists to apply successive linearizations around a current estimate and to warp a multiresolution representation of the data accordingly. This approach relies on an image pyramid, constructed by successive low-pass filtering and down sampling of the original images. A large displacement field $\tilde{\mathbf{v}}$ is first estimated at coarse resolution where motion amplitude should be sufficiently reduced in order to make the initial differential data model valid. Then, the estimation is refined through an incremental fields $\mathbf{v}'$ while going down the pyramid [3]. The latter are estimated within a linear scheme by minimizing linearized motion-compensated functionals : for the decomposition $\mathbf{v}^k = \tilde{\mathbf{v}} + \mathbf{v}'$, Eq.34 is linearized around $\tilde{\mathbf{v}}$ and yields to a motion-compensated linear formulation of the data term. Let us denote by $\tilde{\zeta}^k$ the coarse scale divergence estimate div$\tilde{\mathbf{v}}$ and omit for sake of clarity point coordinates $\mathbf{s}$ in the integrals. For the k-th layer, the linearized data term reads $J_d(\mathbf{v}^k, \mathbf{w}^k, \mathbf{w}^{k+1}, h_{obs}^k) =$

$$\int_\Omega \phi_d \{ e^{\tilde{\zeta}^k} ([\tilde{h}_{obs}^k \nabla \tilde{\zeta}^k + \nabla \tilde{h}_{obs}^k]^T \mathbf{v}' + \tilde{h}_{obs}^k) - \mathbb{I}_{C^k}(h_{obs}^k) + g \Delta t f(\tilde{\zeta}^k, \mathbf{w}^k, \mathbf{w}^{k+1}) \} d\mathbf{s} \tag{36}$$

where if $\tilde{\zeta}^k \neq 0$, $f(\tilde{\zeta}^k, \mathbf{w}^k, \mathbf{w}^{k+1}) =$

$$\frac{\rho^k \mathbf{w}^k - \rho^{k+1} \mathbf{w}^{k+1}}{\tilde{\zeta}^k} \left(1 - e^{\tilde{\zeta}^k} + \mathbf{v}' \nabla \tilde{\zeta}^k \left(\frac{e^{\tilde{\zeta}^k} - 1}{\tilde{\zeta}^k} - e^{\tilde{\zeta}^k} \right) \right)$$

and if $\tilde{\zeta}^k = 0$, $f(\tilde{\zeta}^k, \mathbf{w}^k, \mathbf{w}^{k+1}) = \rho^{k+1} \mathbf{w}^{k+1} - \rho^k \mathbf{w}^k$.

In order to enhance the estimation accuracy, the two-stage estimation scheme (introduced in section 3.3) including correlation-based constraints and *a priori* information on mesoscale atmosphere dynamics can constitute an alternative approach to common multi-resolution. In the first stage of such an estimation scheme, the vertical motion component is neglected as the estimation performs at large scales (of order of 100 km). As a matter of fact, in this stage, large scale displacement estimation relies on the (2D) ICE model. Moreover, large displacements are constrained by a collection of correlation-based vectors and a sound temporal smoother. In the second refinement stage acting at fine scale (of order of 1 km), the correlation-based constraints together with the temporal smoother are disconnected and the (2D) ICE model is replaced by the 3D ICE model. This second stage implies the use of the motion-compensated expression of Eq. 36.

4.2.3   Minimization issues

In the proposed optimization scheme, we chose to minimize a discretize version of functionals of Eq. 36 and Eq. 35. Let us denote by z^k the robust weights associated to the semi-quadratic penalty function

related to the data term. Minimization is done by alternatively solving large systems for unknowns $\mathbf{v}^k$, $\mathbf{w}^k$ and z^k through a multigrid Gauss-Seidel solver. More explicitly, all variables are first initialized to zero. A global optimization procedure is then successively operated at each level of the multiresolution pyramid. This procedure first performs in a multigrid optimization strategy, the minimization with respect to $\mathbf{v}^k$ of a linearized functional composed of the data term defined in Eq.36 and of the second order smoothness term defined in Eq.35. As variables $\{\mathbf{w}^k\}$ and $\{z^k\}$ are first frozen, this first step can be performed independently for each layer level $k \in [1, K]$. Once the minima have been reached, in a second step, fixing variables $\{\mathbf{v}^k\}$ and $\{z^k\}$, the same functional is minimized with respect to each $\mathbf{w}^k, k \in [2, K]$. Note that vertical wind $\mathbf{w}^k$ is estimated considering variables related to the layer above the boundary $\{\mathbf{w}^{k+1}, h_{obs}^k, \tilde{h}^k, \mathbf{v}^k, z^k\}$ and the layer underneath the boundary $\{\mathbf{w}^{k-1}, h_{obs}^{k-1}, \tilde{h}^{k-1}, \mathbf{v}^{k-1}, z^{k-1}\}$. Finally, in a last step for each pixel locations and for each $k \in [1, K]$, the robust weights z^k are in turn updated while variables $\{\mathbf{v}^k\}$ and $\{\mathbf{w}^k\}$ are kept fixed. The three previous minimization steps are iterated until a global convergence criterion is reached, that is to say until the variation of the estimated solution between two consecutive iterations becomes sufficiently small.

It is important to point out that the proposed 3D estimation methodology does not increase much the complexity of the original non-linear horizontal motion estimation problem. Indeed, given horizontal motion, the vertical wind estimation constitutes a linear quadratic problem which can be efficiently solved.

4.3 Experimental evaluation

4.3.1 Synthetic image sequence

For an exhaustive evaluation, we have relied on a simulated flow of an atmosphere decomposed into $K = 3$ layers corresponding to low, medium and high clouds. The resulting synthetic images have been chosen to simulate a layered atmosphere contracting itself at its basis, driven by ascendant winds, and expanding itself at its top. Let us describe the 3D motion simulation. A real cloud classification map (used in the next experiment) has been employed to dissociate the layers, and to assign them to different image regions C^k. Thus, for each layers k, a sparse image $h_{obs}^k(t)$ of 128 by 128 pixels has been generated, representative of cloud pressure difference measurements on the assigned regions C^k and of a fixed saturation value on the complementary domain. A textured image of mean 600 hPa and with a standard deviation of 100 hPa has been used to simulate cloud pressure difference values. The three resulting images are presented in figure 9. An horizontal motion $\mathbf{v}^1$ issued from a divergent sink has been imposed to the lower layer, while on the middle layer no horizontal winds $\mathbf{v}^2 = 0$ has been considered. On the higher layer, a motion $\mathbf{v}^3$ issued from a divergent source has been applied. The latter sink and
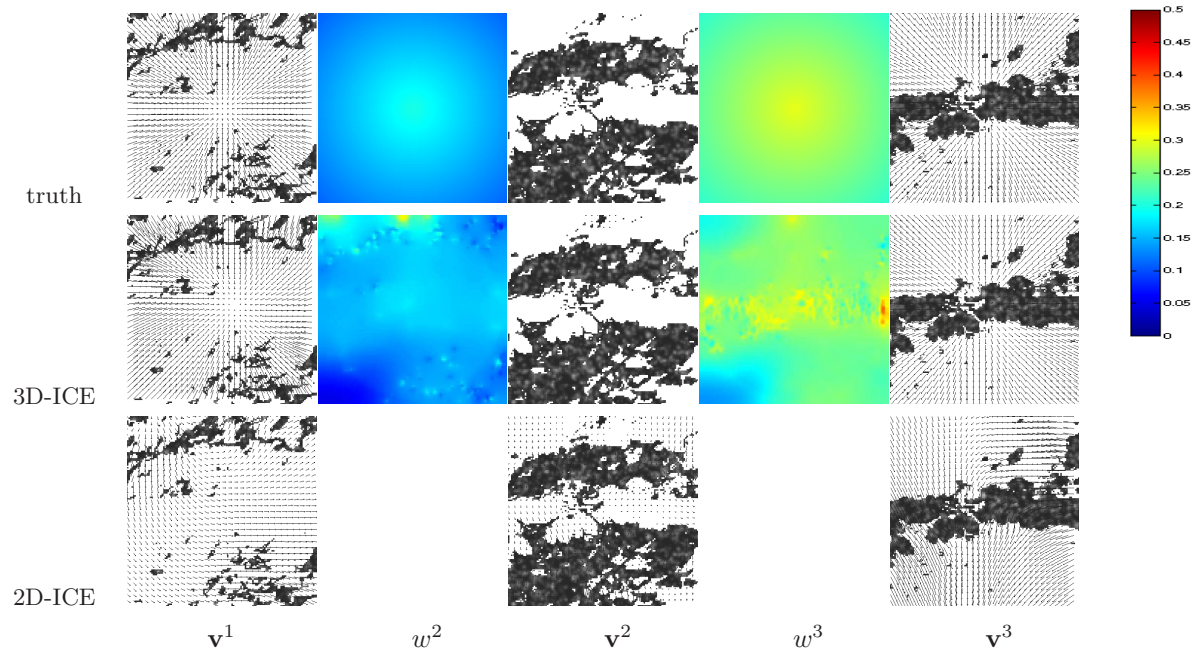
Figure 9: ***Recovery of horizontal*** $\{\mathbf{v}^1, \mathbf{v}^2, \mathbf{v}^3\}$ ***and vertical*** $\{w^2, w^3\}$ ***wind fields.*** *Simulated 3D winds (1st line). Horizontal winds related to the high (left), the medium (middle) and the low (right) layer are superimposed on the cloud pressure difference observations $[h^1_{obs}, h^2_{obs}, h^3_{obs}]$. Horizontal motion estimated with the 3D ICE model (2nd line) have been compared to results obtained with a 2D version of the model (3rd line).*

source possess a decreasing influence while going away from the center of the image to its boundaries (motion amplitudes ranges in the interval $\sim 0 - 1.25$ pixel per frame, that is $\sim 0 - 4\,m.s^{-1}$). Non-uniform vertical winds of strength $w^2 \in [0.1, 0.2]\,m.s^{-1}$ and $w^3 \in [0.2, 0.3]\,m.s^{-1}$ have been simulated on the boundaries shared respectively by the lower and the medium layers, and by the medium and the high layers respectively. The latter horizontal and vertical winds have been used to deform, according to the time integrated 3D-ICE model (Eq.33), image observations $[h^1_{obs}(t), h^2_{obs}(t), h^3_{obs}(t)]$ in order to generate propagated images $[h^1_{obs}(t+\Delta t), h^2_{obs}(t+\Delta t), h^3_{obs}(t+\Delta t)]$ with $\Delta t = 900$ seconds.

Horizontal and vertical winds which have been retrieved with the 3D estimator can be visualized in figure 9. For the three layer levels, vertical and horizontal winds are accurately estimated in cloudy regions. The estimator accuracy is evaluated in table 12, using for horizontal wind the Barron angular

		Barron's error (degree)	Speed bias (pixel)	RMSE (m/s)
3D-ICE	w^3			0.027
	w^2			0.028
	$\mathbf{v}^3$	6.426	0.099	
	$\mathbf{v}^2$	0.138	0.002	
	$\mathbf{v}^1$	3.566	0.058	
2D-ICE	$\mathbf{v}^3$	29.608	0.210	
	$\mathbf{v}^2$	6.331	0.112	
	$\mathbf{v}^1$	38.276	0.161	

Figure 10: **Numerical evaluation**. Barron angular error and speed bias on horizontal winds $\{\mathbf{v}^1, \mathbf{v}^2, \mathbf{v}^3\}$ and RMSE on vertical wind $\{w^2, w^3\}$ provided by the 3D-ICE model. Comparison with horizontal winds produced by a 2D version of the model.

error [1] and the speed bias, and for vertical wind the Root Mean Square Error (RMSE). In observations free areas, vertical and horizontal winds appear to be consistent with the divergent and ascendant motions. Note that in the latter regions, the estimator acts as a 3D wind extrapolator. Moreover, it can be noticed that the proposed layer interacting model increases significantly the estimation performances. In particular, the convergent motion of the lower layer is well characterized although only very few observations are available. For comparison purpose we have run on this sequence the same estimator imposing a zero value to the unknown vertical components. This comes to use the 2D layered data model as proposed in [9]. As a result, this estimator calculates independent horizontal winds for the three different layers in the very same numerical implementation setup as for the 3D wind estimator. Results which are presented in figure 9 and in table 12 show that the latter estimator completely fails to accurately characterize horizontal motion. This demonstrates that, although vertical wind $(\sim 0.1 - 0.3 \, m.s.^{-1})$ is weak compared to horizontal motion $(\sim 0 - 4 \, m.s.^{-1})$, its influence can not be neglected in the estimation process. As evaluated in table 10, a 3D data model clearly improves the results in such a situation.

4.3.2 Satellite image sequence

We then turned to qualitative evaluations on a METEOSAT Second Generation meteorological sequence of 4 images acquired at a rate of an image every 15 minutes, with a spatial resolution of 3 kilometers

at the center of the whole Earth image disk. The images of 512 by 200 pixels cover an area over the Gulf Guinea. The images are EUMETSAT top of cloud pressure observations which are associated to top of cloud classifications [18]. According to section 2, pressure images and classifications maps have been used to derive pressure difference image segments for 3 broad layers, at low, intermediate and high altitude. Figure 11 displays the pressure difference images related to the higher layer, together with the 3D estimated wind fields. One can visualize here large convective systems. They are characterized by strong ascendant flows which are smoothly reversed after bursting while reaching the tropopause cover. Such scenarios have been correctly estimated as shown in figure 11. Furthermore, let us remark that the time-consistency and the correct range of wind values estimated are a testimony of the stability of the 3D estimation method.
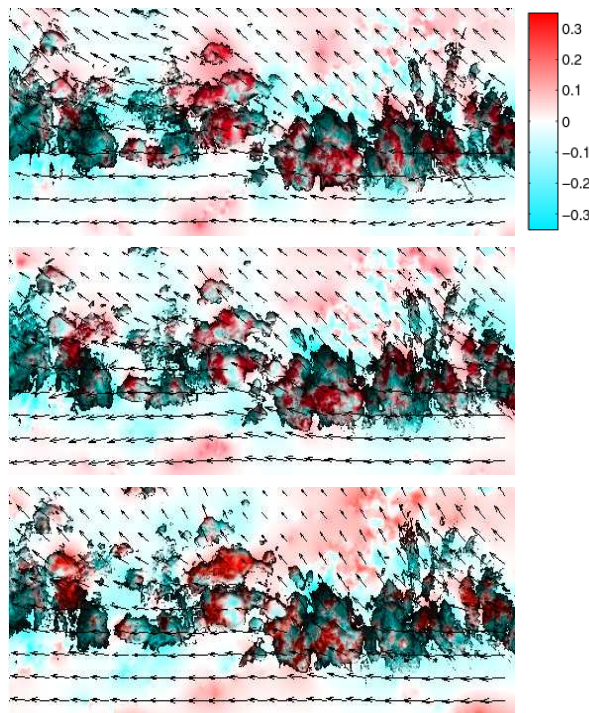

Figure 11: **Estimation of 3D wind in atmospheric convective systems.** *Cloud pressure difference images of the highest layer at 3 consecutive times (from top to bottom). Estimated horizontal wind vectors which have been plotted on the images range in the interval* $[0, 10]\, m.s.^{-1}$. *Retrieved vertical wind maps on the highest layer lower boundary have been superimposed on the pressure difference images with a shaded red color for ascendant motion and a shaded blue color for descendant motion. Vertical wind ranges in the interval* $[-0.5, 0.5] m.s.^{-1}$.

5 Large mesoscale estimation of 2D winds by image assimilation with shallow-water model

We now propose to use the exact shallow-water formulation of the Navier-Stokes equations to control the motion evolution across the sequence. This is done through data assimilation which combines the *a priori* exact dynamic and the pressure difference observations obtained from satellite images.

5.1 Data assimilation principle

5.1.1 Introduction

Data Assimilation is a technique related to optimal control theory which allows estimating over time the state of a system of variables of interest [2, 6, 15, 27]. This method enables a smoothing of the unknown variables according to an initial state of the system, a dynamic law and noisy measurements of the system's state.

Let $\mathcal{V}$ be a Hilbert space identified to its dual defined over Ω. The evolution of the state variable $X \in \mathcal{W}(t_0, t_f) = \{f | f \in L^2(t_0; t_f; \mathcal{V}\}$ is assumed to be described through a (possibly non linear) differential dynamical model $\mathbb{M} : \mathcal{V} \mapsto \mathcal{V}$:

$$\left\| \begin{array}{l} \partial_t \boldsymbol{X}(\boldsymbol{x}, t) + \mathbb{M}(\boldsymbol{X}(\boldsymbol{x}, t)) = 0 \\ \boldsymbol{X}(t_0) = \boldsymbol{X}_0 \end{array} \right. \tag{37}$$

where $\boldsymbol{X}_0$ is a control parameter. We then assume that noisy observations $Y \in \mathcal{O}$ are available, where $\mathcal{O}$ is another Hilbert space. These observations may live in a different space (a reduced space for instance) from the state variable. We will nevertheless assume that there exists a differential operator $\mathbb{H} : \mathcal{V} \mapsto \mathcal{O}$, that goes from the variable space to the observation space. A least squares estimation of the control variable regarding the whole sequence of measurements available within a considered time range $[t_0; t_f]$ comes to minimize with respect to the control variable $\boldsymbol{X}_0 \in \mathcal{V}$, a cost function of the following form:

$$J(\boldsymbol{X}_0) = \frac{1}{2} \int_{t_0}^{t_f} ||Y - \mathbb{H}\boldsymbol{X}(\boldsymbol{X}_0, t)||_R^2 \, dt, \tag{38}$$

where R is the covariance matrix of the observations Y.

A first approach consists in computing the functional gradient through finite differences. Denoting N the dimension of the control parameter $\boldsymbol{X}_0$, such a computation is impractical for control space of large dimension since it requires N integrations of the evolution model for each required value of the gradient functional. *Adjoint models* as introduced first in meteorology by Le Dimet and Talagrand in [15] authorize

the computation of the gradient functional in a single backward integration of an adjoint variable. The value of this adjoint variable at the initial time provides the value of the gradient at the desired point. This first approach is widely used in environmental sciences for the analysis of geophysical flows [15, 27].

5.1.2 Differentiated model

To obtain the adjoint model, the system of equations (37) is firstly differentiated with respect to a small perturbation $d\boldsymbol{X} = \frac{\partial \boldsymbol{X}}{\partial \boldsymbol{X}_0} d\boldsymbol{X}_0$:

$$\left\| \begin{array}{l} \partial_t d\boldsymbol{X}(\boldsymbol{x},t) + \partial_{\boldsymbol{X}}\mathbb{M}d\boldsymbol{X} = 0 \\ d\boldsymbol{X}(t_0) = d\boldsymbol{X}_0 \end{array} \right. \tag{39}$$

where $\partial_{\boldsymbol{X}}\mathbb{M}$ is the tangent linear operator of $\mathbb{M}$ defined by its gâteaux derivative. The gradient of the functional in the direction $d\boldsymbol{X}_0$ must also be computed:

$$\begin{aligned} \left\langle \frac{\partial J}{\partial \boldsymbol{X}_0}, d\boldsymbol{X}_0 \right\rangle &= \int_{t_0}^{t_f} \left\langle (Y - \mathbb{H}\boldsymbol{X}(\boldsymbol{X}_0)), \mathbb{H}\frac{\partial \boldsymbol{X}}{\partial \boldsymbol{X}_0} d\boldsymbol{X}_0 \right\rangle_R dt \\ &= \int_{t_0}^{t_f} \langle \mathbb{H}^* R(Y - \mathbb{H}\boldsymbol{X}(\boldsymbol{X}_0)), d\boldsymbol{X} \rangle_{\mathcal{V}} \, dt, \end{aligned} \tag{40}$$

where $\mathbb{H}^*$ is the adjoint operator of $\mathbb{H}$ defined by:

$$\forall X \in \mathcal{V}, Y \in \mathcal{O}; \langle X, \mathbb{H}Y \rangle_{\mathcal{V}} = \langle \mathbb{H}^* X, Y \rangle_{\mathcal{O}}.$$

5.1.3 Adjoint model

We then introduce the adjoint variable $\lambda \in \mathcal{W}(t_0, t_f)$. The first equation of the differentiated model (39) is multiplied by this adjoint variable and integrated in the time interval $[t_0; t_f]$:

$$\int_{t_0}^{t_f} \langle \partial_t d\boldsymbol{X}(\boldsymbol{x},t) + \partial_{\boldsymbol{X}}\mathbb{M}d\boldsymbol{X}, \lambda \rangle_{\mathcal{V}} = 0.$$

After an integration by parts, we have:

$$\int_{t_0}^{t_f} \langle -\partial_t \lambda + \partial_{\boldsymbol{X}}\mathbb{M}^* \lambda, d\boldsymbol{X}(\boldsymbol{x},t) \rangle_{\mathcal{V}} \, dt = \langle \lambda(t_0), d\boldsymbol{X}(t_0) \rangle_{\mathcal{V}} - \langle \lambda(t_f), d\boldsymbol{X}(t_f) \rangle_{\mathcal{V}}, \tag{41}$$

where the adjoint operator $\partial_{\boldsymbol{X}}\mathbb{M}^*$ is defined by:

$$\forall X, Y \in \mathcal{V}; \quad \langle X, \partial_{\boldsymbol{X}}\mathbb{M}Y \rangle_{\mathcal{V}} = \langle \partial_{\boldsymbol{X}}\mathbb{M}^* X, Y \rangle_{\mathcal{V}}.$$

To perform the computation of the gradient functional, we assume that $\lambda(t_f) = 0$ and define the following adjoint problem:

$$\left\|\begin{array}{l} -\partial_t \lambda + \partial_{\boldsymbol{X}} \mathbb{M}^* \lambda = \mathbb{H}^* R(Y - \mathbb{H}\boldsymbol{X}(\boldsymbol{X}_0)) \\ \lambda(t_f) = 0. \end{array}\right. \tag{42}$$

5.1.4 Functional gradient

Combining (40), (41) and (42), we finally obtain the gradient functional as:

$$\frac{\partial J}{\partial \boldsymbol{X}_0} = \lambda(t_0). \tag{43}$$

Hence, assimilation principle enables to compute the functional gradient with a single backward integration. In the next section, we adapt this process to the control of high dimensional state variables, characterizing the dynamics of layered atmospheric flows.

5.2 Application to atmospheric layer motion estimation

5.2.1 Shallow-water model

In order to provide a dynamical model describing the evolution of the behavior of pressure difference observations, we use the shallow-water approximation (horizontal motion much greater than vertical motion under the assumption of incompressibility) [23]. This approximation is valid for the upper range of mesoscale analysis in a layered atmosphere. Therefore, considering horizontal scales of order of 100 km, combined with layer depths of order of 1 km, makes the shallow-water approximation relevant.

Sallow-water approximation assumes incompressibility. Thus we consider a constant density $\overline{\rho}^k$ within the layer, which implies under hydrostatic balance that horizontal divergence is weak. Let us remark that this incompressibility simplification which underlies a shallow water system is reasonable, while it may be erroneous for finer horizontal scales. Mean densities $\overline{\rho}^k$ can be related to the average pressures $\overline{p}^k$ by vertical integration of the equation of state for dry air ($p = \rho R T$) combined with the hydrostatic relation

$(dp = -g \int \rho dz)$ under the assumption of constant lapse rate $(T = T_0 + \gamma z)$ where g, R, T_0 and γ denote physical constants. More precisely, between altitudes z_0 and z (or pressure p_0 and p), one obtains :

$$\int_{p_0}^{p} \frac{dp'}{p'} = - \int_{z_0}^{z} \frac{g}{R(T_0 + \gamma z')} dz', \tag{44}$$

which yields after some calculation to the expression of density as a function of pressure [12]:

$$\rho(p) = \frac{p_0}{RT_0} \Big(\frac{p}{p_0}\Big)^{\frac{\gamma R}{g}+1}. \tag{45}$$

Thus, computing the vertical average, the mean density related to the k-th layer reads :

$$
\begin{aligned}
\overline{\rho}^k &= \frac{1}{\overline{p}^{k+1} - \overline{p}^k} \int_{\overline{p}^k}^{\overline{p}^{k+1}} \rho(p) dp \\
&= \frac{p_0^2}{(\overline{p}^{k+1} - \overline{p}^k)(\frac{\gamma R}{g} + 2)RT_0} \Big[\Big(\frac{p}{p_0}\Big)^{\frac{\gamma R}{g}+2}\Big]_{\overline{p}^k}^{\overline{p}^{k+1}}.
\end{aligned} \tag{46}
$$

Note that a constant lapse rate γ, that is to say a linear variation of temperature with altitude, is a rough approximation in the troposphere. However, as we are averaging the obtained density law vertically and horizontally over the whole domain embedding the layer, the impact of such an assumption should have minor impact on the modeling.

We now derive a shallow-water model dedicated to atmospheric layers. Expanding the total derivatives in the isobaric coordinate system (x, y, p) and using the fact that the flow is incompressible (zero local 3D divergence), Eq .18 can be rewritten as :

$$
\begin{cases}
\frac{\partial u}{\partial t} + \frac{\partial u^2}{\partial x} + \frac{\partial uv}{\partial y} + \frac{\partial u\omega}{\partial p} + \frac{p_x}{\rho_0} - vf^\phi &= 0 \\
\frac{\partial v}{\partial t} + \frac{\partial uv}{\partial x} + \frac{\partial v^2}{\partial y} + \frac{\partial v\omega}{\partial p} + \frac{p_y}{\rho_0} + uf^\phi &= 0
\end{cases} \tag{47}
$$

where we recall that ω denotes the vertical wind component in pressure coordinates.

In order to perform the vertical integration of Eq. 47 and Eq. 9 in the pressure interval $[p(s^{k+1}), p(s^k)]$, we use the boundary conditions of Eq. 10. To achieve such a vertical integration in the pressure interval $[p(s^{k+1}), p(s^k)]$ varying with spatial coordinates, we employ the Leibnitz formula with the previous boundary conditions. Thus, using Eq. 10 and Eq. 11, the vertical integration of Eq. 47 in the pressure interval $[p(s^{k+1}), p(s^k)]$ yields to a momentum conservation equation for the k-th atmospheric layer :

$$\frac{\partial(\mathbf{q}^k)}{\partial t} + \text{div}\Big(\frac{1}{h^k}\mathbf{q}^k \otimes \mathbf{q}^k\Big) + \frac{1}{2\overline{\rho}^k}\nabla_{xy}(h^k)^2 + \begin{bmatrix} 0 & -1 \\ 1 & 0 \end{bmatrix} f^\phi \mathbf{q}^k = 0 \tag{48}$$

with

$$\mathbf{q}^k = h^k \mathbf{v}^k, \tag{49}$$

$$\text{div}(\frac{1}{h^k}\mathbf{q}^k \otimes \mathbf{q}^k) = \begin{bmatrix} \frac{\partial(h^k(u^k)^2)}{\partial x} + \frac{\partial(h^k u^k v^k)}{\partial y} \\ \frac{\partial(h^k u^k v^k)}{\partial x} + \frac{\partial(h^k(v^k)^2)}{\partial y} \end{bmatrix}, \tag{50}$$

And by vertical integration of the continuit equation of Eq. 9 in the pressure interval $[p(s^{k+1}), p(s^k)]$, we supplement the momentum conservation law of Eq. 48 by the mass conservation law of Eq. 12, and obtain independent shallow-water equation systems for atmospheric layers $k \in [1, K]$:

$$\begin{cases} \frac{\partial h^k}{\partial t} + \text{div}(\mathbf{q}^k) = 0 \\ \frac{\partial(\mathbf{q}^k)}{\partial t} + \text{div}(\frac{1}{h^k}\mathbf{q}^k \otimes \mathbf{q}^k) + \frac{1}{2\bar{\rho}^k}\nabla_{xy}(h^k)^2 + \begin{bmatrix} 0 & -1 \\ 1 & 0 \end{bmatrix} f^\phi \mathbf{q}^k = 0, \end{cases} \tag{51}$$

Note that as we are in the isobaric coordinate system, partial derivatives with respect to x, y and t are defined at constant pressure p. However, according to section 2, pressure difference observations correspond to rough constant pressure interval. Therefore, such data fit the shallow water model of Eq. 51 defined in the isobaric coordinate system.

Equation 51 is discretized spatially with non oscillatory schemes [30] and integrated in time with a third order Runge-Kutta scheme. Note that this equation system describes the dynamics of physical quantities expressed in standard units. Thus, some dimension factors appear in the equation when it is discretized on a pixel grid with velocities expressed in pixels per frame and pressure in hecto pascal hPa. As one pixel represents Δx meters and one frame corresponds to Δt seconds, the densities $\overline{\rho}^k$ expressed in pascal by square seconds per square meter ($Pa\ s^2/m^2$) must be multiplied by $10^{-2}\Delta x^2/\Delta t^2$, and coriolis factor f^ϕ expressed per seconds must be multiplied by Δt. By a scale analysis and as also observed in our experiments, for $\Delta t = 900$ seconds, the third term of equation 48 has a magnitude similar to other terms if $\Delta x \geq 25$km. This is in agreement with the shallow water assumption.

This expression is discretized spatially with non oscillatory schemes [30] and integrated in time with a third order Runge-Kutta scheme. This equation system describes the dynamics of physical quantities expressed in standard units. Thus, some dimension factors appear in the equation when it is discretized on a pixel grid with velocities expressed in pixels per frame and pressure in hecto pascal hPa. As one pixel represents Δx meters and one frame corresponds to Δt seconds, the densities $\overline{\rho}^k$ expressed in pascal by square seconds per square meter ($Pa\ s^2/m^2$) must be multiplied by $10^{-2}\Delta x^2/\Delta t^2$, and coriolis factor

f^ϕ expressed per seconds must be multiplied by Δt. By a scale analysis and as also observed in our experiments, for $\Delta t = 900$ seconds, the third term of equation 48 has a magnitude similar to other terms if $\Delta x \geq 25$km. This is in agreement with the shallow water assumption.

5.2.2 Assimilation of layer motion and pressure differences

We can now define all the components of the assimilation system allowing the recovery of pressure difference observations obtained from section 2.2 through the dynamical model presented in section 5.2.1. The final system enables the tracking of pressure difference h^k and average velocities $\mathbf{q}^k$ related to the set of $k \in [1, K]$ layers. Referring to section 5.1, we then have $X^k = [h^k, \mathbf{q}^k]^T$. The evolution model $\mathbb{M}$ is given by the mesoscale dynamics (51). The only observations available are the pressure difference maps h^k_{obs}. For each layer k, the observation operator then reads: $\mathbb{H} = [1, 0]$ and the process minimizes:

$$J_k(h^k_0, \mathbf{q}^k_0) = \int_{t_0}^{t_f} ||h^k_{obs} - h^k(h^k_0, \mathbf{q}^k_0, t)||^2_{R^k} dt, \tag{52}$$

through a backward integrations of the adjoint model $(\partial_X \mathbb{M})^*$ defined by:

$$\begin{cases} -\partial_t \lambda^k_h(t) + \mathbf{v}^k \cdot (\mathbf{v}^k \cdot \nabla) \lambda^k_\mathbf{q} - \frac{h^k}{\varrho^k} \mathrm{div}(\lambda^k_\mathbf{q}) & = & R^k(h^k_{obs}(t) - h^k(t)), \\ -\partial_t \lambda^k_\mathbf{q}(t) - (\mathbf{v}^k \cdot \nabla) \lambda^k_\mathbf{q} - (\nabla \lambda^k_\mathbf{q}) \mathbf{v}^k - \nabla \lambda^k_h + \begin{bmatrix} 0 & 1 \\ -1 & 0 \end{bmatrix} f^\phi \lambda^k_\mathbf{q} & = & 0, \\ \lambda^k_h(t_f) & = & 0, \\ \lambda^k_\mathbf{q}(t_f) & = & 0. \end{cases} \tag{53}$$

In this expression, λ^k_h and $\lambda^k_\mathbf{q}$ are the two components of the adjoint variable λ^k of layer k [13]. More details on the construction of adjoint models can be found in [27]. One can finally define a diagonal covariance matrix R^k using the mask of observation C^k:

$$R^k(\mathbf{s}, \mathbf{s}) = \begin{cases} = \alpha & if & \mathbf{s} \in C^k \\ = 0 & if & \mathbf{s} \in \bar{C}^k, \end{cases} \tag{54}$$

where α is a fixed parameter (set to 0.1 in our applications) defining the observation covariances. However, as observations are sparse, a nine-diagonal covariance matrix is employed to diffuse information in a 3x3 pixel vicinity. As the assimilation process is not insured to reach a global minima, results depend on initialization. Thus, state variables h^k_0 are initialized with a constant value while initial values for variables $\mathbf{q}^k_0$ are provided by an optic-flow algorithm dedicated to atmospheric layers [9].

5.3   Results

5.3.1   Synthetic experiments

For an exhaustive evaluation, we have relied on image observations generated by short time numerical simulation of atmospheric layer motion according to shallow-water dynamical model (Eq. 51). Realistic initial conditions on layer pressure function and motion have been chosen to derive a synthetic sequence of 10 images. The sequence has then been deteriorated by different noises and by a masking operation to form 4 different data sets. The two first synthetic image sequences named e_1 and e_2 are thus composed of dense observations of h_{obs}^k in hecto-pascal units (hPa) corrupted by Gaussian noises with standard deviation respectively equal to 10 and 20% of the pressure amplitude. A real cloud classification map (used in the next experiment) has been employed to extract regions of data sets e_1 and e_2 in order to create two noisy and incomplete synthetic sequences e_3 and e_4 (see figure 13). For initializing the assimilation system, we have not relied on an optic-flow algorithm in this synthetic case. We have used instead known values of variables h_0^k and $\mathbf{q}_0^k$ deteriorated by Gaussian noises. Results of the joint motion-pressure estimation performed by image assimilation are evaluated in table 12.

	Mask	Noise %	h_{obs}^k RMSE (hPa)	final h^k RMSE (hPa)	initial $|\mathbf{v}_0^k|$ RMSE (pixel/frame)	final $|\mathbf{v}_0^k|$ RMSE (pixel/frame)
e_1		10	15.813880	5.904791	0.22863	0.03457
e_2		20	22.361642	8.133384	0.21954	0.05078
e_3	x	10	15.627055	6.979769	0.22351	0.04978
e_4	x	20	22.798671	10.930078	0.21574	0.05944

Figure 12: **Numerical evaluation**. Decrease of the Root Mean Square Error (RMSE) of estimates h^k and $|\mathbf{v}_0^k|$ by image assimilation for noisy (experiments e_1, e_2, e_3 and e_4) and sparse observations (experiments e_3 and e_4).

It clearly appears that for noisy observations, the assimilation process induces a significant decrease of the RMSE between real and estimated velocities and pressure. Moreover, this table evaluates and demonstrates the efficiency of the proposed estimator for incomplete and noisy observations for both estimating dense motion fields and reconstructing pressure maps h^k. Examples of reconstruction for experiments e_2 and e_3 are presented in figure 13.
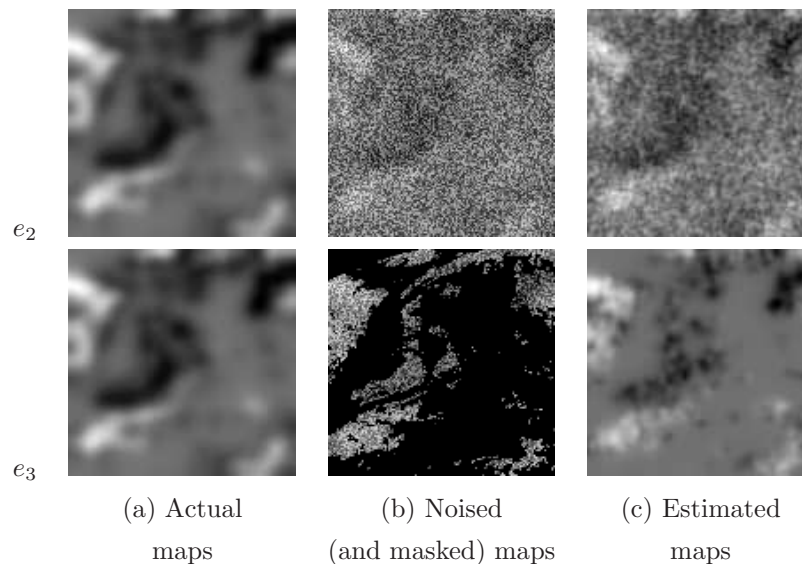
| | (a) Actual maps | (b) Noised (and masked) maps | (c) Estimated maps |

Figure 13: **Synthetic sequences**: Results of experimentations e_2 and e_3, where the pressure maps have been noised (e_2 and e_3) and masked (e_3).

5.3.2 Real meteorological image sequence

We then turned to qualitative comparisons on a real meteorological image sequence. The benchmark data was composed by a sequence of 10 METEOSAT Second Generation (MSG) images, showing top of cloud pressures with a corresponding cloud classification sequence. The 1024×1024 pixel images cover an area over the north Atlantic Ocean during part of one day (5-June-2004), at a rate of one image every 15 minutes. The spatial resolution is 3 kilometers at the center of the whole Earth image disk. Clouds from a cloud-classification were used to segment images into $K = 3$ broad layers, at low, intermediate and high altitude. In order to make the layering assumption valid, low resolution observations on an image grid of 128×128 pixels are obtained by smoothing and sub-sampling for each layer the original data.

By applying the methodology described in section 5.2.2 to the image at this coarser resolution, average motion and pressure difference maps are estimated from the image sequence for these 3 layers. Estimated vector fields superimposed on observed pressure difference maps are displayed in figure 14 for each of the 3 layers. The motion fields estimated for the different layers on the cloudy observable parts are consistent with the visual inspection of the sequence. In particular, several motion differences between layers are very relevant. For instance, near the bottom left corner of the images, the lower layer possesses a southward

motion while the intermediate layer moves northward. Moreover, the temporal coherence of the retrieved motion demonstrates the efficiency of this spatio-temporal method under physical constraints.

6   Conclusion and perspectives

We have presented three different atmospheric motion estimation methods.

The two first approaches tackle the problem of fine mesoscales layered mesoscale estimation of atmospheric motion. In order to manage incomplete observations, physical knowledge on 3D mass conservation in atmospheric layers have been introduced within optical flow schemes. This yields to 3D atmospheric motion estimated from frame to frame. A two-stage estimation scheme including temporal smoothing and correlation-based constraints has been introduced for time-consistency and large displacements of fine structures.

The last estimator uses an exact shallow-water physical model valid at the upper range of mesoscales. It uses a variational assimilation scheme. This process estimates time-consistent motion fields related to the layer components while performing the reconstruction of dense pressure difference maps. The merit of the joint motion-pressure estimator by image assimilation is that it manages incomplete and noisy observations using *a priori* non linear physical laws for time-consistent estimations across the whole image sequence.

The extension of the large mesoscales image assimilation to a high resolution scheme using a global 3D dynamic model able to capture layer interactions via vertical winds is our next step towards a more complete characterization of distribution of three-dimensional atmospheric winds.

References

[1] Barron, J., Fleet, D., and Beauchemin, S. (1994). Performance of optical flow techniques. *Int. J. Computer Vision*, 12(1):43–77.

[2] Bennet, A.: Inverse Methods in Physical Oceanography. Cambridge University Press (1992)

[3] J. Bergen, P. Burt, R. Hingorani, and S. Peleg. A three-frame algorithm for estimating two-component image motion. *IEEE Trans. Pattern Anal. Machine Intell.*, 14(9):886–895, Sept. 1992.

[4] M. Black and P. Anandan. The robust estimation of multiple motions: Parametric and piecewise-smooth flow fields. *Computer Vision and Image Understanding*, 63(1):75–104, 1996.

[5] T. Corpetti and E. Mémin and P. Pérez : Dense Estimation of Fluid Flows. IEEE Trans. on PAMI vol 24, number 3, pp 365-380 (2002)

[6] Courtier, P., Talagrand, O.: Variational assimilation of meteorological observations with the direct and adjoint shallow-water equations. Tellus **42** (1990) 531–549

[7] J. Fitzpatrick. The existence of geometrical density-image transformations corresponding to object motion. *Comput. Vision, Graphics, Image Proc.*, 44(2):155–174, Nov. 1988.

[8] U. Frisch. *Turbulence : the legacy of A.N. Kolmogorov.* Cambridge university press, 19.

[9] P. Heas, E. Memin, N. Papadakis, A. Szantai *Layered estimation of atmospheric mesoscale dynamics from satellite imagery.* to appear in IEEE trans. on Geoscience and Remote sensing

[10] P. Heas, E. Memin. *3D motion estimation of atmospheric layers from image sequences.* in revision by IEEE trans. on Geoscience and Remote sensing

[11] P. Holland and R. Welsch. Robust regression using iteratively reweighted least-squares. *Commun. Statis.-Theor. Meth.*, A6(9):813–827, 1977.

[12] Holton, J.: An introduction to dynamic meteorology. Academic press (1992)

[13] Honnorat, M., Le Dimet, F.X., Monnier, J.: On a river hydraulics model and Lagrangian data assimilation. In: International Conference on Adaptive Modeling and Simulation, ADMOS'05, Barcelona (2005)

[14] Horn, B., Schunck, B.: Determining optical flow. Artificial Intelligence **17** (1981) 185–203

[15] Le Dimet, F.X., Talagrand, O.: Variational algorithms for analysis and assimilation of meteorological observations: theoretical aspects. Tellus (1986) 97–110

[16] Leese, J., Novack, C., Clark, B.: An automated technique for obtained cloud motion from geosynchronous satellite data using cross correlation. Journal of applied meteorology **10** (1971) 118–132

[17] B. Lucas and T. Kanade. An iterative image registration technique with an application to stereovision. In *Int. Joint Conf. on Artificial Intel. (IJCAI)*, pages 674–679, 1981.

[18] H. Lutz. Cloud processing for meteosat second generation. Technical report, European Organisation for the Exploitation of Meteorological Satellites (EUMETSAT), Available at : http://www.eumetsat.de, 1999.

[19] N. N. Mansour, J. H. Ferziger, and W. C. Reynolds. Large-eddy simulation of a turbulent mixing layer. Technical report, Report TF-11, Thermosciences Div., Dept. of Mech. Eng., Standford University, 1978.

[20] N. Papadakis, P. Heas, E. Memin Image assimilation for motion estimation of atmospheric layers with shallow-water model. In *8th Asian Conference on Computer Vision (ACCV)*, 2007.

[21] P. Ruhnau, A. Stahl, and C. Schnoerr. On-line variational estimation of dynamical fluid flows with physics-based spatio-temporal regularization. In *28th Symposium of the German Association for Pattern Recognition*, Berlin, Sept. 2006.

[22] P. Sagaut. *Introduction a la simulation des grandes echelles pour les ecoulements de fluide incompressible.* Springer Verlag, Collection : Mathematiques et applications 30, 1998.

[23] de Saint-Venant, A.: Théorie du mouvement non-permanent des eaux, avec application aux crues des rivières et l'introduction des marées dans leur lit. C. R. Acad. Sc. Paris **73** (1871) 147–154

[24] Schmetz, J., Holmlund, K., Hoffman, J., Strauss, B., Mason, B., Gaertner, V., Koch, A., Berg, L.V.D.: Operational cloud-motion winds from meteosat infrared images. Journal of Applied Meteorology **32**(7) (1993) 1206–1225

[25] J. Smagorinsky. General circulation experiments with the primitive equations. *Monthly Weather Review*, 91(3):99–164, 1963.

[26] D. Suter. Motion estimation and vector splines. In *Proc. Conf. Comp. Vision Pattern Rec.*, pages 939–942, Seattle, USA, June 1994.

[27] Talagrand, O., Courtier, P.: Variational assimilation of meteorological observations with the adjoint vorticity equation. I: Theory. J. of Roy. Meteo. soc. **113** (1987) 1311–1328

[28] G. Taylor. The transport of vorticity and heat through fluids in turbulent motion. In *Proc London Math Soc. Ser A*, pages 151–421, 1932.

[29] J. Weickert and C. Schnörr. Variational optic-flow computation with a spatio-temporal smoothness constraint. *J. Mathematical. Imaging and Vision*, 14(3):245–255, 2001.

[30] Xu, Z., Shu, C.W.: Anti-diffusive finite difference weno methods for shallow water with transport of pollutant. Journal of Computational Mathematics **24** (2006) 239–251

[31] J. Yuan, C. Schnoerr, and E. Memin. Discrete orthogonal decomposition and variational fluid flow estimation. *Journ. of Mathematical Imaging and Vison*, (accepted for publication), 2006.

[32] Zhou, L., Kambhamettu, C., Goldgof, D.: Fluid structure and motion analysis from multi-spectrum 2D cloud images sequences. In: Proc. Conf. Comp. Vision Pattern Rec. Volume 2., Hilton Head Island, USA (2000) 744–751
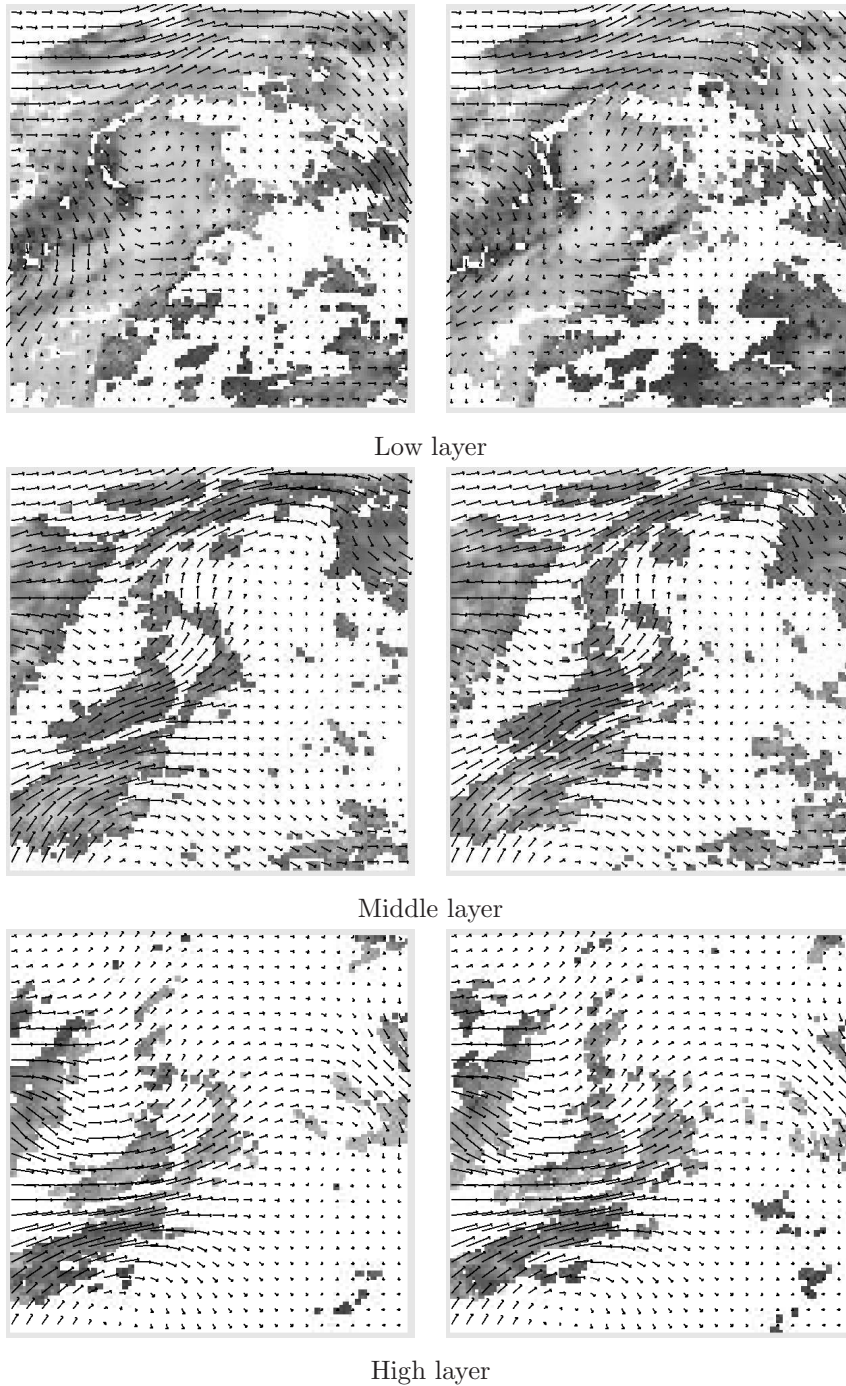
Low layer

Middle layer

High layer

Figure 14: First (left) and last (right) estimated horizontal wind fields superimposed on observed pressure difference maps (original images have been subsampled into images of 128×128 pixels).